JOURNAL OF PETROLOGY | VOLUME 54 | NUMBER 10 | PAGES 1963–1995 | 2013 | doi:10.1093/petrology/egt038

Multi-stage Evolution of Late Neogene Mantle-derived Magmas from the Central Andes Back-arc in the Southern Puna Plateau of Argentina

A. RISSE[1]*, R. B. TRUMBULL[1]†, S. M. KAY[2], B. COIRA[3] AND R. L. ROMER[1]

[1]GFZ GERMAN RESEARCH CENTRE FOR GEOSCIENCES, TELEGRAFENBERG 14473 POTSDAM, GERMANY
[2]DEPARTMENT OF EARTH AND ATMOSPHERIC SCIENCES, CORNELL UNIVERSITY, SNEE HALL, ITHACA, NY 14853, USA
[3]CONICET, CASILLA DE CORREO 258 (4600), S.S. DE JUJUY, ARGENTINA

RECEIVED AUGUST 24, 2012; ACCEPTED JUNE 10, 2013
ADVANCE ACCESS PUBLICATION JULY 19, 2013

The late Miocene and younger mafic back-arc lavas in the southern Puna of the central Andean plateau have been attributed to the aftermath of crustal and mantle lithospheric delamination or foundering. In this paper, we analyze in more detail the nature of the back-arc mafic suite magmas, including the conditions of magma generation in the mantle and of magma evolution during ascent and ponding in the crust, using extensive compositional data for phenocryst minerals and olivine-hosted melt inclusions in combination with published and new whole-rock chemical and isotopic data. We estimate that the primary melts last equilibrated with an enriched mantle source at temperatures near 1375°C and pressures near 2 GPa, which is near the base of the seismically determined ~60 km thick crust. A mantle source geochemically enriched by continental material introduced through delamination and subducted erosion processes is required to explain the coincidence of the high $^{87}Sr/^{86}Sr$ ratios (>0·705) and high Sr concentrations (>700 ppm) of the most primitive lavas (e.g. 9–10 wt % MgO, olivine Fo_{88}). The crystallization conditions inferred from mineral–melt equilibria indicate that olivine (T = 1320–1220°C) was followed by clinopyroxene (T = 1230–1140°C). Clinopyroxene–melt equilibration pressures of 0·7 to near 1 GPa in the most mafic samples indicate that the magmas crystallized at mid-crustal depths of 20–35 km, within a region of inferred partial melt accumulation based on the presence of low seismic velocity zones. Olivine-hosted melt inclusions indicate relatively dry melts (maximum 0·5 wt % H_2O) with unusual high-Al basaltic compositions, which are attributed to the high-pressure suppression of plagioclase crystallization. A first stage of crustal contamination before mid-crustal accumulation and crystallization of the mafic magmas is suggested by high O-isotope ratios in olivine phenocrysts and negative Eu anomalies in clinopyroxene from the plagioclase-free mafic lavas. Mixing models based on trace elements and radiogenic isotopes suggest assimilation of silicic melt in the lower crust, similar to contemporaneous glassy dacites with steep REE patterns and negative Eu anomalies. A second stage of crustal assimilation at shallower depths is indicated by the mismatch of incompatible elements in clinopyroxene relative to bulk-rock compositions, by strong positive correlations of radiogenic isotopes with wt % SiO_2, and by petrographic observation of partly resorbed and reacted quartz xenocrysts. Mixing calculations require the erupted magmas to have assimilated in total some 15–25% crust.

KEY WORDS: *back-arc magmatism; Central Andes; geothermobarometry; melt inclusions; LA-ICP-MS; isotopes; clinopyroxene*

INTRODUCTION

The Puna Plateau in NW Argentina is part of the Andean Central Volcanic Zone (CVZ), and is of special interest geodynamically as a 'type locality' for the concept of

†Corresponding author. Telephone: +49-331-2881495. E-mail: bobby@gfz-potsdam.de
*Present address: Bavarian Environment Agency, 95030 Hof, Germany.

© The Author 2013. Published by Oxford University Press. All rights reserved. For Permissions, please e-mail: journals.permissions@oup.com

continental crustal and mantle lithospheric delamination beneath compressional orogens with consequent asthenospheric upwelling and enhanced heat input into the crust (Kay & Kay, 1993; Kay *et al.*, 1994). The northern Puna Plateau has a variable crustal thickness of about 50–65 km (e.g. Yuan *et al.*, 2002; McGlashan *et al.*, 2008), which is some 10 km thinner than the Altiplano crust to the north (Yuan *et al.*, 2002), yet it has a higher average elevation (e.g. Whitman *et al.*, 1996). The mismatch between crustal thickness and elevation in the Puna Plateau compared with the Altiplano has led to suggestions of dynamic isostatic uplift in the Puna owing to a hotter upper mantle (Isacks, 1988). Other evidence in support of the delamination model includes the geophysical characteristics of the mantle that are consistent with high temperature: low seismicity and high attenuation of seismic waves (e.g. Whitman *et al.*, 1992, 1996; Liang *et al.*, 2011; Bianchi *et al.*, 2013), a late Neogene shift in the stress regime from horizontal compression to oblique transtension (Marrett *et al.*, 1994; Allmendinger *et al.*, 1997), and an abundance of late Neogene mafic volcanism (e.g. Coira *et al.*, 1993; Kay *et al.*, 1994, 1999). Contemporaneous with the mafic volcanism in this region is one of the largest silicic ignimbrite calderas in the central Andes, Cerro Galán. Hybrid magmas from the Galán center represent significant crustal melting, which has likewise been regarded as a result of enhanced mantle temperatures and melting (Francis *et al.*, 1989; Kay *et al.*, 1994, 2011). The high liquidus temperatures for mafic back-arc magmas determined in this study (up to 1320°C) provide further evidence for asthenospheric upwelling under the southern Puna.

The significance of late Neogene mafic volcanism as a window into the mantle beneath the southern Puna Plateau has been long recognized; several studies have addressed the geochemistry and petrogenesis of the magmas and their time–space distribution with respect to the geodynamic setting (Knox *et al.*, 1989; Coira *et al.*, 1993; Kay *et al.*, 1994, 1999; Kraemer *et al.*, 1999; Risse *et al.*, 2008; Kay & Coira, 2009; Drew *et al.*, 2009). These studies employed whole-rock major and trace element and isotopic analyses and their focus was on the nature of the mantle and crustal materials making up the magma source(s). The aim of this study is to provide new constraints on the conditions of magma generation, storage and evolution in the crust under the southern Puna Plateau using whole-rock geochemical data (new and compiled from the literature) combined with analyses of olivine and clinopyroxene phenocrysts and their included phases. Pressure and temperature (P–T) conditions for magma crystallization during ascent and storage are derived from mineral–melt equilibria. These P–T constraints are combined with trace element data for clinopyroxene phenocrysts, melt inclusions and bulk-rocks to determine at what stage(s) in ascent and magma evolution crustal assimilation took place. The combined data suggest a two-stage history of magma modification by fractionation and assimilation, with an early stage in the lower crust and a second stage during magma pooling at mid-crustal depths, the latter being supported by seismological evidence.

GEODYNAMIC SETTING

One of the first-order tectonic aspects of the Central Volcanic Zone (CVZ) in the Andes is the variable dip angle of the subducting Nazca plate along the cordillera, which is well constrained by seismicity (e.g. Cahill & Isacks, 1992) and which also has its expression in the time–space distribution of arc volcanic activity (Coira *et al.*, 1993; Kay *et al.*, 1999; Kay & Coira, 2009). North of about 24°S, the slab dips 25–30° beneath the continental margin and it shallows progressively southward, more rapidly so at the northern boundary of the 'flat-slab' region at 28–33°S, where arc volcanism ceased about 6 Myr ago (e.g. Kay & Abruzzi, 1996). The area of our study is at the southern end of the CVZ between 25 and 27°S (Fig. 1), where volcanism since the early Miocene has produced three major volcanic associations: stratovolcanoes, silicic ignimbrites and monogenetic mafic centers (Coira *et al.*, 1993; Kay *et al.*, 1994; Kay & Coira, 2009). The stratovolcano association comprises early Miocene to Pleistocene composite centers that build up the frontal volcanic arc of the Western Cordillera and extend into the back-arc plateau region in the vicinity of transverse lineaments (e.g. Alonso *et al.*, 1984; Coira *et al.*, 1993; Richards & Villeneuve, 2002). Prominent examples in the southern Puna region are the Antofalla, Beltrán and Tebenquicho volcanoes (Fig. 1). The ignimbrite association in the southern Puna includes a large number of medium- to small-scale (<100 km^3) silicic ignimbrites and domes whose ages range from Miocene to Pleistocene (Coira & Pezzutti, 1976; Siebel *et al.*, 2001; Schnurr *et al.*, 2007; Kay *et al.*, 2010). More prominent than these are the very large-volume (>1000 km^3) ignimbrites from the Cerro Galán caldera complex (Fig. 1), which was active from about 6 to 2 Ma (Sparks *et al.*, 1985; Francis *et al.*, 1989; Folkes *et al.*, 2011; Kay *et al.*, 2011). The small and compositionally simple (monogenetic), mafic volcanoes and lava fields in the back-arc region, referred to here as the 'mafic suite', range in age from late Miocene to Pleistocene (Risse *et al.*, 2008). The largest concentration of these is in the southern Puna, but there are also scattered occurrences in the northern Puna (Déruelle, 1991; Coira & Kay, 1993), and further north in the Bolivian Altiplano (Davidson & de Silva, 1995; Hoke & Lamb, 2007).

Southern Puna mafic volcanism

Late Neogene mafic volcanism in the southern Puna is concentrated in the region around the Salars de Antofalla and de Hombre Muerto, and extends southward into the

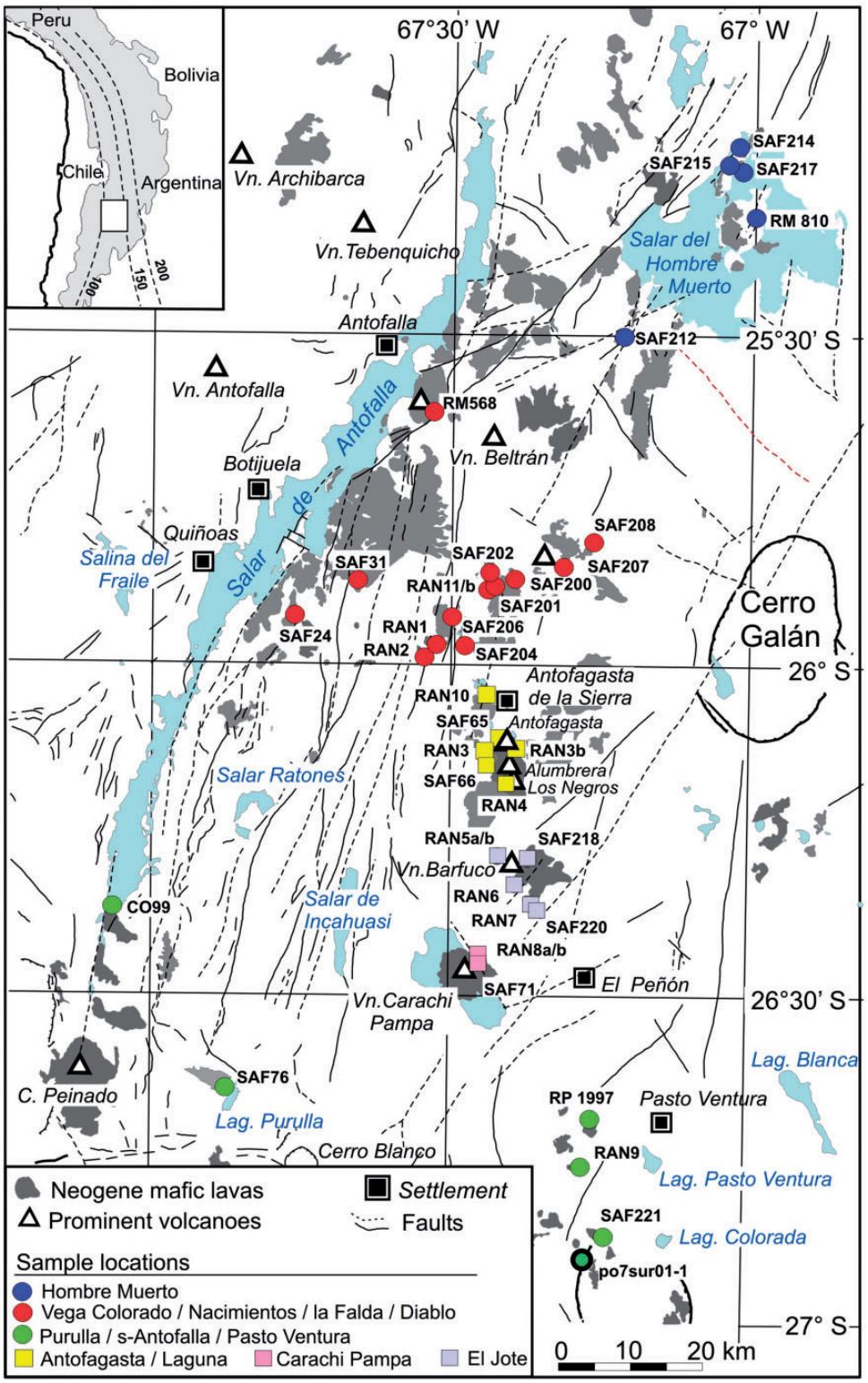

Fig. 1. Geological map of the study area, modified from Risse *et al.* (2008), showing the distribution of Neogene mafic eruptive rocks and important faults and lineaments (from Schnurr *et al.*, 2006).

Pasto Ventura region (Fig. 1). Typical volcanic features are small (<2 km^3) lava flows and cinder cones, some with aprons of ash and lapilli deposits scattered with larger clasts. The lavas are typically aphyric or weakly porphyritic (olivine ± clinopyroxene; see below), and commonly vesicular. It has long been recognized that the mafic lavas in the southern Puna erupted along NNE–SSW-trending faults, and that many of the faults underwent a change in kinematics from compression to strike-slip or oblique extension. From the limited dates on the mafic volcanism then available, early studies placed this change in the late Pliocene (Allmendinger, 1986; Marrett *et al.*, 1994; Allmendinger *et al.*, 1997). Newer geochronology results and compilations by Kay *et al.* (1999) and Risse *et al.* (2008) have shown that volcanism along these faults in fact commenced in the late Miocene (7 Ma), suggesting at least local extension by this time (e.g. Schoenbohm & Strecker, 2009). Risse *et al.* (2008) also noted a spatial pattern of ages suggesting an early and continued focus of activity at the eastern margin of the Salar de Antofalla near the Archibarca lineament, with younger and less extensive activity spreading to the north and south. The timing of mafic volcanism in the southern Puna overlaps with the waning activity at the composite stratovolcanoes Archibarca, Tebenquicho and Beltrán (Coira *et al.*, 1993; Kay *et al.*, 1999; Kraemer *et al.*, 1999; Richards *et al.*, 2006), and corresponds closely to the ignimbrite eruptions from Cerro Galán, from about 6 to 2 Ma (Sparks *et al.*, 1985; Kay *et al.*, 2011).

The most common rocks in the back-arc mafic suite are basaltic andesites and basaltic trachyandesites, with minor amounts of basalt, trachybasalt, and andesite. Knox *et al.* (1989) and Kay *et al.* (1994) distinguished three compositional series based on incompatible trace element ratios [rare earth elements (REE), La/Ta, Ba/Ta] and K_2O contents. The most common and widespread is the calc-alkaline (CA) series, distinguished by relatively high ratios of La/Ta (>25) and Ba/Ta (>300), which is interpreted as having a strong influence of fluid-transported components from the subducted slab. The within-plate (WP) series has relatively low values of the La/Ta and Ba/Ta ratios, suggesting minor influence of slab-derived components in the source. The within-plate series is restricted geographically to the central part of the back-arc region, west of Cerro Galán (Kay *et al.*, 1994). The third, shoshonitic series is distinguished by high K_2O contents. It occurs farther north in the back-arc region, between 24 and 25°S latitude, and is not represented among the samples collected for this study.

SAMPLE DISTRIBUTION AND ANALYTICAL METHODS

Samples

This study is based on 33 representative samples from the southern Puna mafic suite that were chosen based on the presence of olivine and/or clinopyroxene phenocrysts. Of these, 28 contain phenocrysts suitable for estimating the *P–T* conditions of crystallization. The sample set contains an approximately equal number from the within-plate and calc-alkaline groups, the locations cover the entire area of the back-arc suite (Fig. 1), and the ages span the range of back-arc mafic activity, from 4·6 to less than 0·1 Ma.

Bulk-rock analyses

To ensure a coherent dataset, new analyses of major and trace elements (Ba, Cr, Ni, Rb, Sr, V, Y, Zn and Zr) were performed on most samples at the GFZ Potsdam by X-ray fluorescence (XRF; Siemens SRS 303 with a Rh tube). All whole-rock samples were crushed and powdered using standard jaw crusher and agate milling equipment. Ferric iron was determined by titration potentiometry (after Wilson, 1955), and analyses of H_2O and CO_2 were made by infrared spectrometry (LECO RC-412). Additional trace elements (Nb, Ta, Cs, Hf, Pb, Th, U and the REE) were analyzed by inductively coupled plasma mass spectrometry (ICP-MS; Perkin Elmer/SCIEX ELAN 5000A), as described by Dulski (2001). Rock compositions are reported in Table 1.

Procedures for the new isotopic analysis of Sr, Nd and Pb at the GFZ laboratories have been described in detail by Romer *et al.* (2005). Isotope ratio measurements of Sr were made on Ta filaments with a VG SECTOR 54-30; Nd and Pb isotope ratios were measured with a Finnigan MAT262, with a double (Re) filament technique for Nd and single (Re) filament for Pb. Both Sr and Nd analyses were measured using dynamic multi-collection, whereas Pb analyses were carried out in static mode. Measured Sr and Nd ratios were normalized to $^{86}Sr/^{88}Sr = 0{\cdot}1194$ and $^{146}Nd/^{144}Nd = 0{\cdot}7219$, respectively. Analyses of the Sr and Nd reference materials NBS SRM987-Sr and La Jolla-Nd in the period of this study yielded average values for $^{87}Sr/^{86}Sr$ of $0{\cdot}710260 \pm 0{\cdot}000006$ (2σ, $n = 10$) and for $^{143}Nd/^{144}Nd$ of $0{\cdot}511850 \pm 0{\cdot}000006$ (2σ, $n = 11$). Mass fractionation of Pb isotope ratios was corrected with a factor of 0·1% per a.m.u. based on repeated measurement of reference material NBS981. The radiogenic isotope results are presented in Table 2. Initial ratios for Sr and Nd were calculated for samples from volcanic centers with known ages (13 of 16 samples). The age correction is insignificant for the time span (4·6–0·03 Ma), and for consistency all plots show the measured isotope ratios.

Electron microprobe analyses

In situ analyses of minerals and glass were made with a CAMECA SX100 electron microprobe at GFZ operated at 15 kV and 10–20 nA beam current. The electron beam was focused to 2–5 μm for mineral analyses, whereas for glass a defocused beam of about 10 μm was used. Special care was taken to assess the reliability of glass analyses.

Table 1: Whole-rock composition of samples from the back-arc mafic suite

Sample:	RM568*	RM810*	RAN1	RAN2	RAN3	RAN4	RAN5a	RAN6	RAN7	RAN8a	RAN9	RAN10	RAN11b	SAF24*	SAF32*	SAF65*	SAF71*
Group:	WP	WP	WP	WP	trans	WP	WP	trans	trans	WP	CA	CA	CA	WP	CA	CA	WP
Latitude (S):	25·634	25·402	25·974	25·992	26·117	26·152	26·293	26·334	26·363	26·457	26·707	26·032	25·868	25·930	25·882	26·130	26·473
Longitude (W):	67·566	67·038	67·538	67·543	67·423	67·427	67·409	67·385	67·372	67·428	67·246	67·445	67·416	67·760	67·665	67·429	67·416
Phenocryst %:	5	6	5	7	8	4	6	4	n.d.	5	6	5	8	8	3	7	n.d.
SiO_2	55·3	55·5	53·6	53·2	53·5	52·1	51·7	51·5	51·5	51·2	50·2	53·2	56·5	52·2	53·7	53·3	52·0
TiO_2	1·20	1·20	1·02	1·12	1·40	1·98	1·38	1·32	1·41	1·42	1·22	1·25	1·35	1·37	1·32	1·84	1·90
Al_2O_3	16·2	15·9	14·1	14·7	16·2	15·8	14·9	15·2	15·2	15·9	14·7	14·9	16·0	15·4	16·6	15·9	15·3
Fe_2O_3	n.d.	n.d.	1·61	1·63	1·55	1·24	1·93	2·34	2·07	1·45	4·75	3·31	1·36	n.d.	n.d.	n.d.	n.d.
FeO	7·7	7·1	5·83	5·93	5·88	6·87	5·83	5·55	6·01	6·53	3·72	3·94	5·62	7·7	8·1	8·0	8·41
MnO	0·1	0·1	0·13	0·13	0·12	0·13	0·14	0·13	0·13	0·13	0·15	0·11	0·10	0·2	0·1	0·1	0·12
MgO	6·2	6·7	9·72	9·30	6·97	6·93	9·02	9·00	8·83	7·29	9·27	6·79	5·20	8·3	7·1	7·2	8·75
CaO	6·4	7·4	7·53	7·30	6·91	6·93	7·90	8·17	7·69	8·18	8·87	8·49	6·33	8·2	8·3	7·5	7·70
Na_2O	3·1	3·2	2·80	2·91	3·38	3·51	3·27	3·12	3·19	3·67	3·40	3·42	3·34	3·4	3·5	3·5	3·66
K_2O	1·81	1·94	1·60	1·74	2·07	2·39	2·04	1·79	1·77	1·68	1·76	1·97	2·29	1·73	1·68	1·73	1·44
P_2O_5	n.d.	n.d.	0·24	0·27	0·32	0·47	0·42	0·34	0·32	0·36	0·48	0·49	0·30	0·36	0·25	0·27	0·32
CO_2	n.d.	n.d.	0·07	0·08	0·06	0·10	0·08	0·06	0·07	0·18	0·11	0·29	0·06	n.d.	n.d.	n.d.	n.d.
H_2O^+	n.d.	n.d.	0·71	0·89	0·83	0·79	0·56	0·73	0·80	0·82	0·60	1·05	1·15	n.d.	n.d.	0·48	0·11
Total	98·1	99·1	99·0	99·2	99·2	99·2	99·1	99·2	99·0	98·7	99·3	99·2	99·5	98·8	100·7	99·7	99·7
Cs	1·90	2·70	1·57	1·66	1·89	1·86	2·75	1·77	1·70	0·98	0·46	1·60	1·57	1·6	1·4	2·0	1·36
Rb	n.d.	n.d.	42	46	59	56	60	51	51	42	45	49	66	n.d.	n.d.	66	45
Sr	515	495	511	531	556	665	691	695	637	645	966	1069	522	542	551	585	743
Ba	430	453	352	394	489	504	505	462	434	420	543	480	476	435	393	521	451
Nb	n.d.	n.d.	15·9	17·7	21·1	34·0	32·0	23·2	22·3	24·6	17·7	14·2	17·9	n.d.	n.d.	n.d.	n.d.
Ta	1·70	1·41	1·09	1·20	1·32	2·20	2·10	1·53	1·45	1·47	1·00	0·82	1·17	1·83	1·01	1·35	1·92
Zr	n.d.	n.d.	141	159	191	234	176	169	175	180	181	167	202	n.d.	n.d.	n.d.	n.d.
Y	n.d.	n.d.	18·7	19·9	19·9	22·6	22·1	21·3	21·7	20·8	22·8	18·9	19·9	n.d.	n.d.	n.d.	n.d.
La	28·4	30·8	24·9	28·4	33·0	39·5	41·3	41·3	36·6	36·5	50·2	55·4	36·6	37·6	28·5	33·9	37·3
Ce	59·4	63·6	50·8	58·3	68·9	82·6	82·4	82·7	75·1	72·9	97·9	115·6	76·8	75·9	58·9	73·7	74·0
Pr	n.d.	n.d.	6·09	7·00	8·36	10·01	9·71	9·47	8·76	8·63	11·33	13·71	9·21	n.d.	n.d.	n.d.	n.d.
Nd	32·6	27·5	24·0	26·9	32·3	39·7	35·9	36·7	34·7	33·2	44·3	50·1	35·3	30·4	30·5	33·2	37·1
Sm	6·19	5·85	4·78	5·33	6·22	7·57	6·64	6·41	6·26	5·16	7·73	7·70	6·74	6·03	6·01	6·41	6·61
Eu	1·44	1·44	1·30	1·39	1·62	2·12	1·81	1·70	1·66	1·70	2·02	1·87	1·63	1·62	1·51	1·72	1·65
Gd	n.d.	n.d.	4·17	4·54	5·08	6·13	5·56	5·39	5·15	5·23	6·12	5·50	5·57	n.d.	n.d.	n.d.	n.d.
Tb	0·80	0·78	0·61	0·67	0·75	0·87	0·80	0·74	0·74	0·75	0·83	0·75	0·80	0·82	0·74	0·81	0·85
Dy	n.d.	n.d.	3·63	3·86	4·11	4·80	4·49	4·22	4·28	4·10	4·64	3·90	4·14	n.d.	n.d.	n.d.	n.d.
Ho	n.d.	n.d.	0·72	0·73	0·78	0·85	0·84	0·78	0·81	0·82	0·86	0·71	0·76	n.d.	n.d.	n.d.	n.d.
Er	n.d.	n.d.	2·01	2·19	2·18	2·36	2·35	2·14	2·26	2·18	2·38	1·95	2·00	n.d.	n.d.	n.d.	n.d.
Tm	n.d.	n.d.	0·29	0·30	0·29	0·32	0·31	0·30	0·29	0·28	0·32	0·26	0·27	n.d.	n.d.	n.d.	n.d.
Yb	1·80	1·93	1·92	1·97	1·91	2·06	2·07	1·94	1·92	1·95	2·05	1·59	1·70	2·13	2·05	2·05	2·21
Lu	0·25	0·27	0·28	0·29	0·28	0·29	0·31	0·30	0·29	0·30	0·30	0·23	0·25	0·26	0·26	0·28	0·30
Hf	4·10	4·43	3·38	3·88	4·86	5·47	4·27	3·92	4·14	4·26	4·59	4·16	5·16	4·31	4·27	5·26	4·50
Pb	n.d.	n.d.	8·09	9·04	10·31	8·69	9·69	9·57	8·66	7·55	9·89	13·4	10·1	n.d.	n.d.	10·2	7·61
Th	6·50	6·14	4·33	5·16	5·95	6·02	6·62	6·44	5·82	5·53	8·36	8·43	8·21	5·91	5·16	6·22	5·55
U	1·90	1·89	1·07	1·17	1·38	1·46	2·00	1·54	1·44	1·20	1·87	1·59	1·47	1·46	1·39	1·46	1·37
Cr	282	351	553	484	200	175	358	390	352	228	341	293	113	416	323	244	280
Ni	105	113	202	207	129	114	181	192	196	104	159	141	71	166	114	123	121
V	n.d.	n.d.	172	178	192	172	189	191	203	171	219	193	173	n.d.	n.d.	n.d.	n.d.
Zn	n.d.	n.d.	69	76	78	85	71	75	79	77	75	88	92	n.d.	n.d.	n.d.	n.d.

(continued)

Table 1: Continued

Sample:	SAF76	SAF200	SAF201	SAF202	SAF206	SAF207	SAF208	SAF212	SAF214	SAF215	SAF217	SAF218	SAF220	SAF221	RP1997	CO99
Group:	WP	CA	CA	WP	CA	WP	CA	CA	CA	trans	CA	trans	trans	CA	CA	WP
Latitude (S):	26·650	25·872	25·868	25·870	25·926	25·853	25·830	25·508	25·216	25·265	25·245	26·306	26·357	26·407	26·700	26·372
Longitude (W):	67·870	67·393	67·416	67·436	67·489	67·310	67·287	67·219	67·029	67·052	67·048	67·390	67·375	67·249	67·260	68·070
Phenocryst %:	7	4	6	n.d.	n.d.	5	10	n.d.	5	n.d.	n.d.	5	5	n.d.	5	5
SiO_2	54·5	56·8	53·1	53·5	53·0	55·7	54·3	60·5	54·7	52·9	53·2	51·4	51·3	55·3	50·8	52·2
TiO_2	1·31	1·16	1·14	1·28	1·2	1·13	1·29	0·98	1·20	1·18	1·13	1·42	1·42	0·91	1·20	1·16
Al_2O_3	15·4	15·6	15·7	15·8	16·1	14·6	15·5	15·4	15·7	15·6	15·6	15·1	15·3	15·6	15·1	16·1
Fe_2O_3	1·62	1·64	1·99	1·43	2·4	1·79	2·08	0·26	1·74	1·70	1·73	3·32	2·14	2·21	5·42	1·83
FeO	5·63	4·95	5·80	6·51	5·4	4·90	5·34	4·88	5·39	5·93	5·63	4·81	5·98	4·24	2·62	5·68
MnO	0·12	0·10	0·13	0·13	0·13	0·11	0·12	0·08	0·11	0·12	0·12	0·13	0·13	0·12	0·15	0·13
MgO	6·82	5·93	7·54	7·22	7·4	7·86	7·13	4·52	6·60	7·97	7·62	7·82	8·48	6·35	8·38	6·94
CaO	6·92	6·26	7·70	7·52	7·8	6·18	7·19	4·89	6·97	7·58	7·80	8·40	7·81	6·95	8·84	7·91
Na_2O	3·31	3·09	2·73	2·74	2·9	2·59	3·07	3·44	3·01	2·93	2·86	2·94	3·06	3·44	3·54	3·66
K_2O	2·37	2·31	1·82	1·91	1·8	2·54	1·97	2·90	1·76	1·62	1·60	1·83	1·82	2·56	1·95	1·77
P_2O_5	0·32	0·25	0·20	0·21	0·2	0·28	0·29	0·32	0·25	0·22	0·22	0·37	0·30	0·24	0·56	0·25
CO_2	0·14	0·02	0·10	0·04	0·2	0·13	0·05	0·04	0·12	0·20	0·35	0·09	0·11	0·15	0·11	0·09
H_2O^+	0·54	0·85	0·97	0·82	0·9	1·14	0·48	0·49	1·08	0·99	0·85	0·85	0·75	0·71	0·27	0·79
Total	99·0	99·0	98·9	99·1	99·5	99·0	98·8	98·7	98·6	98·9	98·7	98·5	98·7	98·7	98·9	98·5
Cs	2·02	1·44	1·95	2·02	1·5	2·97	1·67	6·78	2·56	2·83	2·46	1·80	1·73	2·36	0·73	2·08
Rb	78	64	51	53	53	79	54	106	65	56·7	56·1	54	54	77·9	53	52
Sr	584	516	432	409	460	533	578	645	489	428	438	624	632	680	1102	559
Ba	483	507	343	319	369	437	395	644	490	401	581	375	447	742	684	418
Nb	27·0	11·9	10·5	13·1	10·3	21·3	13·8	13·9	15·6	14·5	13·7	19·2	25·0	18·2	25·0	21·0
Ta	1·80	0·77	0·67	0·94	0·64	1·60	0·89	1·20	0·88	0·9	0·7	1·20	1·40	1·1	1·20	1·30
Zr	212	206	152	151	150	189	180	225	175	152	151	165	180	165	208	171
Y	22·7	18·1	21·2	23·0	20·6	19·8	20·7	18·4	20·5	20·6	19·8	22·3	21·8	17·3	22·4	20·3
La	42·0	37·5	24·1	21·8	24·2	33·0	31·3	49·1	30·3	23·8	24·5	34·8	36·8	33·2	64·4	29·6
Ce	83·2	75·8	50·8	45·6	50·9	68·0	65·6	98·5	62·8	49·5	51·3	71·4	74·4	65·9	121·4	59·9
Pr	9·40	8·98	6·21	5·71	6·4	8·09	8·11	11·4	7·64	6·13	6·38	8·74	8·80	7·80	13·73	7·10
Nd	35·6	33·9	24·8	23·4	25·1	31·0	32·0	42·2	30·0	24·7	25·3	34·4	34·4	29·9	51·6	27·8
Sm	6·55	6·28	5·19	5·20	5·07	5·79	6·24	7·34	5·98	5·19	5·28	6·59	6·29	5·68	8·69	5·46
Eu	1·70	1·56	1·36	1·38	1·38	1·43	1·60	1·65	1·47	1·35	1·38	1·70	1·65	1·50	2·21	1·50
Gd	5·56	5·24	4·88	5·06	4·71	4·89	5·49	5·48	5·16	4·75	4·72	5·86	5·26	4·66	6·52	5·05
Tb	0·80	0·72	0·71	0·76	0·70	0·73	0·77	0·73	0·73	0·71	0·69	0·81	0·75	0·64	0·84	0·73
Dy	4·55	3·85	4·18	4·44	4·05	3·91	4·25	3·88	4·15	4·09	4·11	4·56	4·38	3·44	4·72	4·10
Ho	0·85	0·70	0·83	0·87	0·80	0·77	0·79	0·70	0·78	0·80	0·78	0·90	0·83	0·66	0·87	0·80
Er	2·43	1·80	2·26	2·38	2·20	2·01	2·19	1·84	2·16	2·18	2·15	2·34	2·29	1·74	2·33	2·16
Tm	0·33	0·24	0·31	0·32	0·31	0·28	0·28	0·26	0·29	0·30	0·30	0·32	0·32	0·25	0·31	0·30
Yb	2·11	1·55	2·04	2·10	1·98	1·82	1·89	1·57	1·85	1·97	1·90	2·01	2·04	1·59	2·02	1·92
Lu	0·31	0·24	0·31	0·32	0·28	0·27	0·28	0·24	0·26	0·28	0·28	0·29	0·30	0·23	0·30	0·28
Hf	5·01	5·27	3·99	3·91	3·88	4·79	4·62	5·70	4·44	3·84	3·95	4·18	4·27	4·32	5·04	4·20
Pb	10·7	13·1	8·76	9·99	8·84	11·7	8·53	17·7	10·8	8·88	9·54	8·36	9·48	13·81	10·4	8·0
Th	9·19	9·06	5·71	4·90	5·93	9·02	6·39	9·74	6·52	5·42	5·53	5·46	6·27	8·97	10·71	5·17
U	2·15	1·73	1·35	1·55	1·22	1·98	1·38	2·92	1·61	1·50	1·56	1·36	1·48	2·59	2·27	1·59
Cr	225	247	383	310	413	343	269	234	274	379	350	329	342	260	278	270
Ni	116	121	133	119	94	172	122	73	85	470	112	135	174	88	133	106
V	154	157	208	210	208	157	190	127	182	206	181	200	191	154	191	179
Zn	70	89	82	78	112	77	84	80	84	78	78	80	78	64	78	73

Groups: WP, within plate (La/Ta <25, Ba/Ta <350); CA, calc-alkaline (La/Ta >30, Ba/Ta >400); trans, transitional characteristics. Latitude and longitude in decimal degrees; phenocryst % values are volume % total phenocrysts, from visual estimates aided by abundance charts. Oxides in wt % by XRF, FeO by titration, H_2O and CO_2 by IR spectroscopy, trace elements in ppm by ICP-MS (Cr, Ni, V, Zn by XRF). n.d., not determined.
*Analysis from Kay *et al.* (1999).

Table 2: Radiogenic isotope composition of selected samples from the back-arc mafic suite

Sample:	SAF200	SAF202	SAF207	SAF212	SAF214	SAF218	SAF65	SAF71	SAF76	CO99	RAN2	RAN9	RAN5a	RAN4	SAF208	RAN10
Age (Ma)	2·50	2·80	2·40	4·60	2·40	3·20	0·30	0·80	0·80	0·60	0·03					
Sm (ppm)	6·28	5·20	5·79	7·34	5·98	6·59	6·04	6·19	6·55	5·46	5·33	7·73	6·64	7·57	6·24	7·70
Nd (ppm)	33·9	23·4	31·0	42·2	30·0	34·4	32·0	33·5	35·6	27·8	26·9	44·3	35·9	39·7	32·0	50·1
$^{143}Nd/^{144}Nd_{(m)}$	0·512372	0·512457	0·512407	0·512332	0·512392	0·512457	0·512498	0·512561	0·512533	0·512564	0·512505	0·512592	0·512598	0·512524	0·512423	0·512403
2σ(mean)	0·000004	0·000004	0·000006	0·000005	0·000006	0·000004	0·000005	0·000005	0·000004	0·000004	0·000005	0·000005	0·000004	0·000005	0·000005	0·000005
$\varepsilon Nd_{(t)}$	−5·2	−3·5	−4·5	−5·9	−4·8	−3·5	−2·7	−1·5	−2·1	−1·4	−2·6	−0·9	−0·8	−2·2	−4·2	−4·6
$\varepsilon Nd_{(0)}$	−5·2	−3·5	−4·5	−6·0	−4·8	−3·5	−2·7	−1·5	−2·1	−1·4	−2·6					
Rb (ppm)	63·9	53·1	78·8	106·1	64·8	54·2	63·6	43·4	78·3	51·6	46·3	44·6	59·6	55·9	54·4	48·6
Sm (ppm)	516	409	533	645	489	624	565	655	584	559	531	966	691	665	578	1069
$^{87}Sr/^{86}Sr_{(m)}$	0·707853	0·707415	0·706910	0·708724	0·707879	0·706693	0·706253	0·705523	0·707898	0·705978	0·705860	0·705266	0·705653	0·705936	0·706830	0·707193
2σ(mean)	0·000005	0·000004	0·000004	0·000011	0·000004	0·000004	0·000004	0·000004	0·000004	0·000004	0·000005	0·000004	0·000004	0·000004	0·000004	0·000004
$^{87}Sr/^{86}Sr_{(i)}$	0·70784	0·70740	0·70690	0·70869	0·70787	0·70668	0·70625	0·70552	0·70790	0·70598	0·70586					
U (ppm)	1·73	1·55	1·98	2·92	1·61	1·36	1·35*	1·21*	2·15*	1·59*	1·17	1·87	2·00	1·46	1·38	1·59
Th (ppm)	9·06	4·90	9·02	9·74	6·52	5·46	6·14*	5·73*	9·19*	5·17*	5·16	8·36	6·62	6·02	6·39	8·43
Pb (ppm)	13·08	9·99	11·70	17·69	10·79	8·36	10·2*	7·61*	10·7*	8·0*	9·04	9·88	9·69	8·69	8·53	13·41
$^{208}Pb/^{204}Pb_{(m)}$	38·98	38·99	39·05	39·03	38·93	38·99	38·87	38·92	39·07	39·03	38·79	39·04	38·98	38·83	38·90	38·84
$^{207}Pb/^{204}Pb_{(m)}$	15·66	15·67	15·69	15·68	15·67	15·67	15·68	15·66	15·67	15·66	15·66	15·65	15·67	15·65	15·67	15·67
$^{206}Pb/^{204}Pb_{(m)}$	18·87	18·95	18·89	18·86	18·84	18·91	18·84	18·88	19·10	19·01	18·82	18·96	19·02	18·80	18·87	18·75

Ages from Risse *et al.* (2008). Initial ratios are not calculated for undated samples, but will be close to measured ratios for ages <10 Ma. Element concentrations determined by ICP-MS (Table 1).

Repeated analyses of basaltic glass USNM 111240 VG-2 ($n = 11$) yielded the following estimates for reproducibility ($\pm 2\sigma$): SiO_2, Al_2O_3, FeO_{tot}, MgO, CaO and Na_2O ~3%; TiO_2 ~5%; K_2O and P_2O_5 ~20%; MnO ~40 wt %.

In situ trace element analyses of clinopyroxene in polished grain mounts were made by laser ablation (LA)-ICP-MS at the University of Frankfurt (analyst Y. Lahaye), using a Merchantek Nd:YAG UV-laser LUV213 and Finnigan ELEMENT2 mass spectrometer (see Lahaye *et al.*, 1997). Internal homogeneity of selected grains was investigated by electron microprobe before ICP-MS analysis. The trace element concentrations were calculated from isotope ratios with reference to Si concentration determined by electron microprobe. Calibration was by the reference glass NIST SRM 612 using values reported by Pearce *et al.* (1997). The estimated uncertainties (1σ) for elements in concentrations <1 ppm are 5–25%, and 5–15% for elements in concentration >1 ppm. From six to 20 spot analyses were made in each sample and outliers were tagged for element values >3 standard deviations of the mean, which could represent interference with unnoticed inclusions. The full dataset is given in Supplementary Data Electronic Appendix 4 (supplementary material is available for downloading at http://www.petrology.oxfordjournals.org).

Devitrified melt inclusions in olivine were re-melted prior to analysis in a Vernadsky-type heating stage, which was flushed with dry He gas to prevent oxidation of the olivine and aid rapid quenching. The heating rates were 50° min^{-1} between 25°C and 1100°C, and 5° min^{-1} thereafter until homogenization. Temperature was calibrated with fine cuttings of Ag (961°C) and Au (1064°C) metal added to the sample grains during runs. After homogenization, grains were mounted individually in epoxy-filled tubes, and selectively polished to expose the inclusions. The melt inclusions were analyzed by electron microprobe for major elements, and a subset was analyzed for trace elements Rb, Sr, Y, Zr, Nb, Th, Ba, and REE by secondary ion mass spectrometry (SIMS) with the Cameca IMS6f instrument at GFZ. Procedures have been described in detail by Kent *et al.* (2002). Operation at 20 nA primary $^{16}O^-$ beam and 12·5 kV accelerating voltage resulted in a beam diameter of about 25 μm. Each analysis consisted of 10 scans of the mass sequence, and element concentrations were calculated based on intensity ratios relative to Ti values determined by electron microprobe, with mass fractionation corrected by measurements of reference glasses KL2-G, ML3B-G (Jochum *et al.*, 2000) and NIST610 (Pearce *et al.*, 1997). Isobaric interference of BaO^+ and REE^+ was corrected after Zinner & Crozaz (1986). Estimated repeatability ($\pm 2\sigma$) is 5–6% for Sr, Zr, Nb, Ba, Y and Ce; about 10% for Rb and La; and 15–20% for Th and the other REE. Melt inclusion water contents were determined by laser Raman spectroscopy at the GFZ (Innova 70–3 Ar^+ laser and Dilor XY Triple 800 mm spectrometer). Concentrations are based on the O–H stretching bands between 3100 und 3750 cm^{-1} calibrated with a series of synthetic hydrous glasses. Procedural details have been given by Thomas (2000), Thomas *et al.* (2006) and Thomas & Davidson (2007).

BULK-ROCK COMPOSITIONS

Major and trace elements

The main compositional features of the southern Puna mafic volcanic rocks have been described in previous studies (Francis *et al.*, 1989; Knox *et al.*, 1989; Kay *et al.*, 1994, 1999; Kraemer *et al.*, 1999; Drew *et al.*, 2009). The samples included in our study are typical of the suite, plotting as trachybasalts, basaltic andesites and basaltic trachyandesites in the total alkalis–silica (TAS) diagram (Fig. 2a). The assignment of samples to the calc-alkaline (CA), within-plate (WP) and transitional groups (Fig. 2b) follows the Kay *et al.* (1994) criteria of La/Ta and Ba/Ta

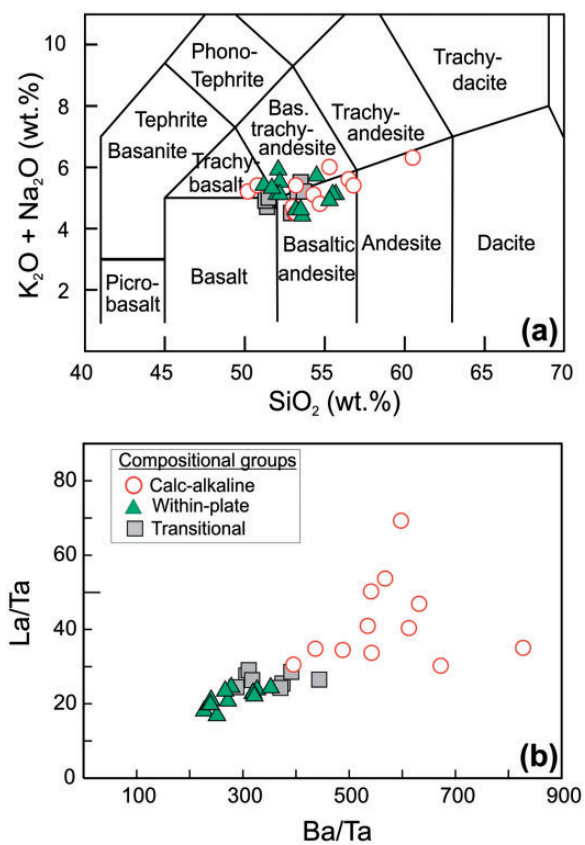

Fig. 2. (a) Total alkalis vs SiO_2 (wt %) for samples from this study, showing rock classification fields after LeBas *et al.* (1986). The symbols denote calc-alkaline, within-plate and transitional compositions based on the criteria of Kay *et al.* (1994). (b) Variation of Ba/Ta vs La/Ta distinguishes calc-alkaline (La/Ta >30, Ba/Ta >400), within-plate (La/Ta <25, Ba/Ta <350) and transitional samples.

ranges as described in the figure caption. The calc-alkaline and within-plate groups are about equally represented. The sample set is in the range of about 50–57 wt % SiO_2, about 5–10 wt % MgO and 57–70 Mg# [100 × molar ratio Mg/(Mg + Fe)]. The volatile contents determined in the bulk-rocks are 0·5–1·1 wt % H_2O and less than 0·3 wt % CO_2 (Table 1). Although the rocks are generally free of alteration and care was taken to remove chips containing filled vesicle material (carbonate and silica) before analysis, the measured volatile contents are probably higher than magmatic values. The measured CO_2 concentrations of 0·1–0·3 wt % exceed the CO_2 solubility in basaltic melts at low pressure (e.g. Holloway & Blank, 1994), and olivine-hosted melt inclusions in sample RAN2 have one-half or less H_2O compared with the bulk sample. The calc-alkaline and within-plate groups show similar compositional ranges for the major and most trace elements, and similar maxima for MgO (9–10 wt %), Ni (150–210 ppm) and Cr (400–550 ppm), which are close to acceptable values for primary magmas. Over the compositional ranges for the sample suite, the major element oxides correlate with MgO, as demonstrated in other studies of these rocks by Kay *et al.* (1994) and Drew *et al.* (2009). We find that these element correlations in the dataset are stronger for the CA series than for the WP series. For example, correlation coefficients (Spearman's rank r') for the CA and WP samples, respectively, are −0·91 vs −0·45 for MgO–SiO_2, 0·86 vs 0·35 for MgO–CaO, and −0·67 vs −0·40 for MgO–K_2O. One reason for the poorer correlations may be mixing with silicic magmas in the mid-crust or assimilation of quartz-rich host-rocks. Quartz xenocrysts rimmed with pyroxene are relatively common in the Puna back-arc rocks (Coira & Kay, 1993); an example is shown in Fig. 3d. Silica assimilation is suggested by the fact that the least-evolved samples RAN1 and RAN2, with >9 wt % MgO, >450 ppm Cr and >200 ppm Ni, have 53·2 and 53·6 wt % SiO_2 (Table 1). The WP samples appear more strongly affected than the

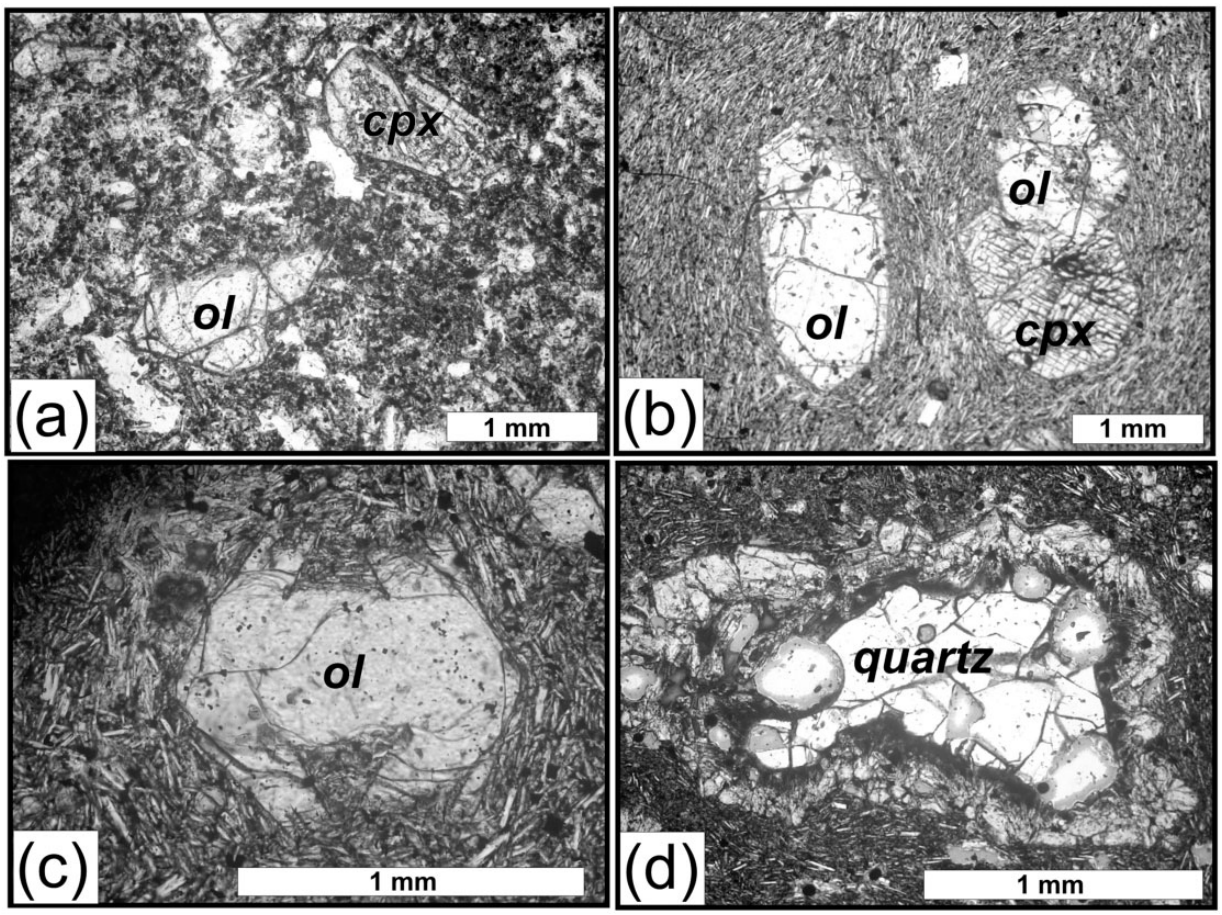

Fig. 3. Representative microphotographs in plane-polarized light showing typical rock textures in the back-arc mafic suite. (a) Sample RP1997 with even-grained texture lacking flow foliation, and phenocrysts of olivine (ol) and clinopyroxene (cpx). (b) Sample SAF208 with a porphyritic texture, flow-oriented plagioclase groundmass and phenocrysts of olivine (ol) and clinopyroxene (cpx). (c) Sample SAF32 with porphyritic texture and flow-oriented felty plagioclase groundmass, with skeletal olivine phenocryst (ol). (d) Sample SAF201 with a partly resorbed quartz xenocryst rimmed with clinopyroxene.

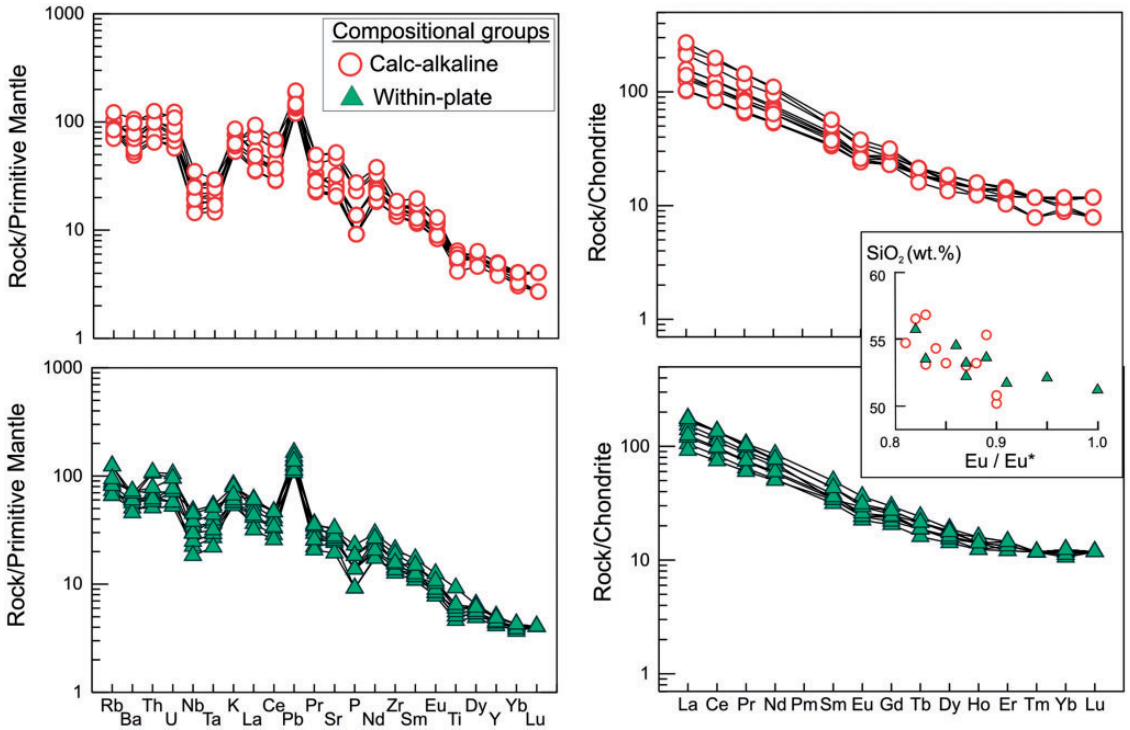

Fig. 4. Summary of trace element characteristics of back-arc mafic suite samples with <57 wt % SiO_2 on normalized multi-element plots [normalization values from Sun & McDonough (1989)]. Left panels show primitive mantle-normalized plots of incompatible elements; right panels show chondrite-normalized REE plots with an inset illustrating the dependence of Eu/Eu* on SiO_2.

CA group, but this may be a coincidence as other indicators of crustal contamination are similar in both groups and their magma temperatures are in the same range (see below).

Summary trace element features of the mafic suite are illustrated as mantle-normalized multi-element and chondrite-normalized REE patterns in Fig. 4. The distinction between the calc-alkaline and within-plate series shows up in deeper negative Nb–Ta troughs at equivalent MgO for the former in the mantle-normalized trace element patterns. This difference is independent of the degree of differentiation (e.g. MgO content) and agrees with the Ba/Ta and La/Ta ratio distinction (see Fig. 2b). Prominent in all samples from both compositional series is the preferential enrichment in Pb relative to neighboring incompatible elements, which provides evidence for crustal assimilation, confirmed by the elevated radiogenic Pb isotope ratios (see below). An important feature for assessing crustal assimilation in the mafic suite is the Eu anomaly. Plagioclase phenocrysts are lacking in these rocks and therefore a negative Eu anomaly is a sign of assimilation rather than plagioclase fractionation (Kay *et al.*, 1994). The ratio Eu_N/Eu^*, where $Eu^* = (Sm_N \times Gd_N)^{0.5}$, is near 1·0 in the most primitive samples and correlates negatively with silica, radiogenic Sr and other indicators of assimilation (inset, Fig. 4), as discussed further below. The Eu anomaly as an index of crustal assimilation is doubly valuable because it can be determined in clinopyroxene phenocrysts and in olivine-hosted melt inclusions, thus providing more insights as to when and where assimilation took place with respect to the magma ascent and crystallization history.

Radiogenic isotopes

Crustal assimilation by mantle-derived magmas has previously been documented in back-arc mafic lavas from the Puna (Francis *et al.*, 1989; Coira & Kay, 1993; Kay *et al.*, 1994, 1999; Drew *et al.*, 2009) as well as from the Bolivian Altiplano (e.g. Davidson & de Silva, 1992). Putting crustal assimilation in the context of magma ascent and evolution is a major focus of this study, and we have determined the radiogenic Sr, Nd and Pb isotopic compositions of 16 of the samples described, which cover the age, geographical and compositional range of the southern Puna mafic suite (Table 2). The new data are within the range of previous studies, as shown in Figs 5 and 6 by the data fields from Kay *et al.* (1994), Kraemer *et al.* (1999) and Drew *et al.* (2009). Because of the young age of the mafic lavas and lack of reliable ages for some of the new and published samples, all isotope ratios are plotted as present-day values for consistency.

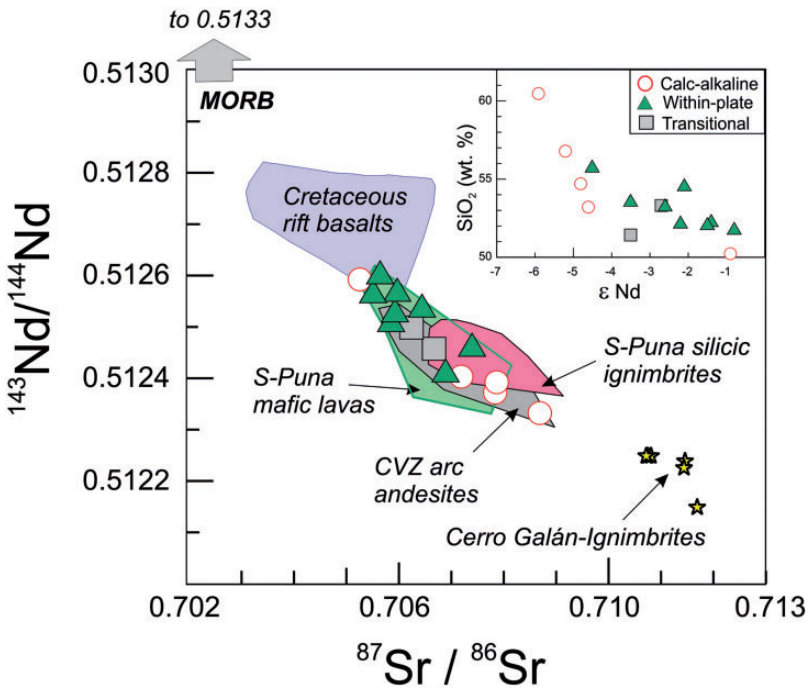

Fig. 5. Sr and Nd isotope ratios of the southern Puna mafic lavas compared with previous data from these rocks (Kay *et al.*, 1994, 1999; Drew *et al.*, 2009). Shown for reference are compositional fields for the arc andesites and small-volume silicic ignimbrites from the southern Central Volcanic Zone (CVZ) compiled by Schnurr *et al.* (2007), large-volume ignimbrites from Cerro Galán (Francis *et al.*, 1989; Kay *et al.*, 2011), and Cretaceous rift basalts (Lucassen *et al.*, 2002). The inset illustrates the correlation of εNd with SiO_2 as evidence that the isotope variations are related to crustal assimilation (see text). All points and data fields represent present-day isotope values.

The $^{87}Sr/^{86}Sr$ ratios range from 0·7053 to 0·7087, and their initial $^{143}Nd/^{144}Nd$ values are 0·51233–0·51260 (εNd = −6·0 to −0·8). The single compositions are shown on a Sr vs Nd isotope diagram against the backdrop of literature values from the CVZ in Fig. 5. Like Kay *et al.* (1994), we find a strong correlation of Sr and Nd initial ratios with silica content (Spearman's rank coefficient = 0·80 for $^{87}Sr/^{86}Sr$, 0·74 for $^{143}Nd/^{144}Nd$) and with the Eu/Eu* ratio, indicating that the isotopic variations within the suite are related to crustal assimilation.

The Pb isotopic compositions of the mafic samples range from 18·75 to 19·10 for $^{206}Pb/^{204}Pb$, from 15·65 to 15·69 for $^{207}Pb/^{204}Pb$ and from 38·83 to 39·45 for $^{208}Pb/^{204}Pb$. Unlike the Nd and Sr isotopic ratios, the Pb isotopic ratios do not correlate with silica or other element concentrations, nor do they show a systematic relationship with the Nd or Sr isotopic ratios in these rocks. An explanation for the independent behavior of Pb isotopes is that most of the Pb in these magmas comes from the continental crust, so that the isotopic ratios are insensitive to varying mantle contributions. The crustal affinity of the Pb isotope compositions in the Puna mafic rocks is underscored by their similarity to the Pb isotope ratios in silicic ignimbrites from nearby Cerro Galán (Kay *et al.*, 2011). The simplest explanation for the crustal affinity of Pb in the mafic rocks is assimilation during magma ascent and evolution in the thick continental crust, although source contamination in the mantle wedge is also possible (see below). In reality, the two processes may act together; however, there are good reasons to favor Pb assimilation in the continental basement. First, Pb isotope ratios in volcanic rocks and ores from the Central Volcanic Zone vary in accord with pre-Andean crustal domains (e.g. Moscoso *et al.*, 1993; Woerner *et al.*, 1992; Mamani *et al.*, 2008), demonstrating that crustal assimilation in the upper plate is the dominant process. Also, the Chile Trench off the CVZ is extremely poor in sediment fill after 10 Ma (Nalpas *et al.*, 2008), and the Pb-isotope composition of Chile Trench sediments (see Fig. 5) is not radiogenic enough to explain the Puna trend.

MINERAL COMPOSITIONS AND GEOTHERMOBAROMETRY

Petrography

The samples that form the basis of this study were chosen for their low degree of differentiation and the presence of olivine and/or pyroxene phenocrysts. The rocks are fine-grained, weakly porphyritic or glomeroporphyritic, with a groundmass containing from nil to ~40 vol. % (devitrified) glass, which is vesicular in many of the samples. Phenocrysts typically make up about 5 vol. % of the rocks (maximum 10 vol. %; see Table 1), with olivine and

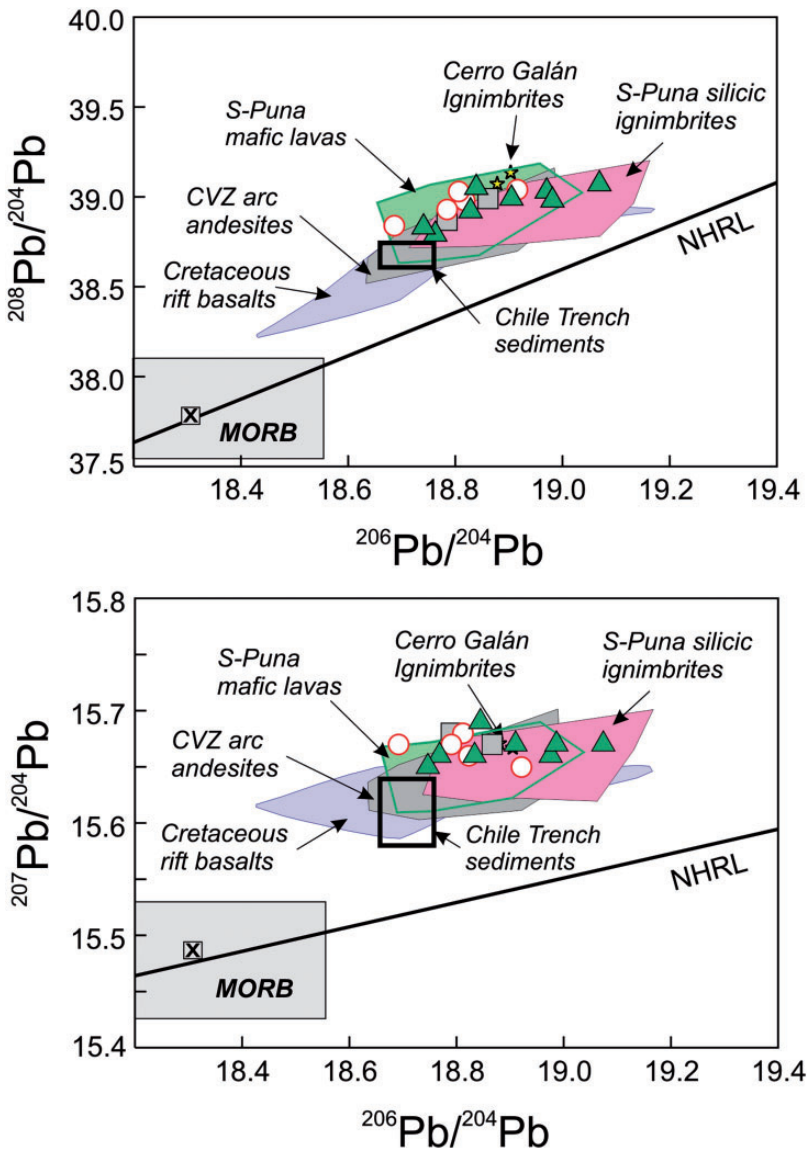

Fig. 6. Pb isotope ratios of the southern Puna mafic lavas compared with fields for other volcanic units in the southern CVZ as explained in Fig. 5. The MORB composition is for glass data from Pacific spreading centers in the PetDB database (www.petdb.org; Lehnert *et al.*, 2000), where × is the mean of ~1600 values and gray box indicates the mean ± 1 standard deviation. The Chile Trench sediment data are from Kilian & Behrmann (2003). NHRL, Northern Hemisphere Reference Line. All points and data fields represent present-day isotope values. Symbols as in Fig. 5.

clinopyroxene as the main phenocryst phases (Fig. 3). Olivine is more abundant than pyroxene in all but the most silicic samples, but there is rarely clear petrographic evidence of the relative order of crystallization. Plagioclase is exclusively a groundmass phase in the mafic lavas, and it commonly defines a flow lineation (Fig. 3b and c). Only the most evolved andesitic rocks (e.g. SAF212 with 60% SiO_2) contain clinopyroxene and plagioclase phenocrysts, as well as minor amounts of orthopyroxene and amphibole. The most abundant groundmass minerals are clinopyroxene, plagioclase, Fe–Ti oxides, and, locally, olivine in the least-evolved rocks. Accessory minerals, which mostly occur as inclusions in these phenocrysts, include chromian spinel, pentlandite, pyrrhotite and apatite.

Olivine

Olivine phenocrysts are euhedral to subhedral and range from ~500 μm to 2 mm in size. Some phenocrysts are zoned, with relatively narrow rims (20–50 μm) having a lower birefringence. Growth zoning in some grains is marked by oriented arrays of inclusions or, more

commonly, by a concentration of inclusions in the central versus the outer parts of the grains. The presence of skeletal olivine in some samples indicates rapid crystallization (Fig. 3c). Olivine phenocrysts commonly include tiny grains of chromian spinel.

Olivine compositions in selected samples are reported in Table 3 and the full dataset is given in Supplementary Data Electronic Appendix 1. The range of phenocryst cores (excluding xenocrysts) is from Fo_{76} to Fo_{89} (Table 3) with those $<Fo_{80}$ being rare. The average core composition is Fo_{84}. Phenocrysts commonly show minor compositional zonation (Fig. 7a), with ~6 mol % (maximum 12 mol %) lower Fo contents in the rims than the cores. Olivine rim compositions overlap those of the groundmass olivine, where present. Single samples commonly have a range of 5–10 mol % Fo in the core compositions, whereby typically the most Fo-rich grains are in equilibrium with the bulk-rock composition given a K_D for Fe–Mg partitioning of $0{\cdot}3 \pm 0{\cdot}04$ (Fig. 7b). Minor constituents in olivine are MnO, with 0·08–0·38 wt % (cores), and CaO, with 0·08–0·26 wt % (cores). Nickel concentrations in the cores range from 0·2 to 0·5 wt % NiO (1570–3930 ppm Ni) and correlate positively with Fo content (Fig. 8a). The highest Ni concentration measured is 0·64 wt % NiO (5030 ppm Ni).

High Ni contents in olivine have been a subject of much interest since Sobolev *et al.* (2007) suggested that high-Ni olivines in basalts indicate an olivine-depleted (pyroxenitic) mantle source. Straub *et al.* (2008) have discussed the possible significance of high-Ni olivines from the basaltic rocks of the Mexican Volcanic Belt, which is a setting not unlike the southern Puna. Those researchers concluded that the mantle source had undergone olivine depletion by reaction with slab-derived hydrous silicic melts. Both the Ni and Fo contents of olivine from the Mexican example are similar to those in our study (Fig. 8a). However, we hesitate to invoke an olivine-depleted mantle in this case because more recent studies by Niu *et al.* (2011) and Putirka *et al.* (2011) have pointed out that the diversity of Ni contents in peridotite melts, and the sensitivity of olivine–melt Ni partitioning to change in T, P and melt MgO are sufficient to permit Ni-rich olivines to crystallize from melts of a mantle source without olivine depletion. We show in Fig. 8b that the Ni in olivines from the southern Puna lavas yields apparent olivine–melt K_D values in reasonable agreement with experimental values, and that the K_D shows the expected inverse correlation with MgO content in the rocks.

Pyroxene

Clinopyroxene (calcic augite) typically forms euhedral to subhedral prismatic phenocrysts 0·2–0·5 mm long, and it is also an abundant phase in the groundmass. The phenocrysts are generally unzoned, and where present, zoning is limited to the outer few microns of the rim. Some phenocrysts display sector zoning. Common inclusions in clinopyroxene are spinel, glass and minor sulfide minerals. Pyroxene compositions for selected samples are reported in Table 4 and the complete data are given in Supplementary Data Electronic Appendix 2. The phenocryst core compositions are in the range $En_{43–52}Wo_{37–45}Fs_{8–13}$, corresponding to a range of Mg# [calculated for Fe^{2+}/Fe^{3+} according to Putirka (2008)] from 72 to 86. Typical variation in Mg# for pyroxene phenocrysts within single samples is around 10, and like olivine, the grains with the highest Mg# are consistent with equilibrium Mg–Fe partitioning ($K_D = 0{\cdot}28 \pm 0{\cdot}07$) with the host-rocks (Fig. 9). Among the important minor constituents in pyroxene, the Al_2O_3 contents vary from 1·4 to 6·9 wt % and correlate positively with Mg#. Maximum values of other elements are 1·1 wt % Cr_2O_3, 1·9 wt % TiO_2, and 0·7 wt % Na_2O. The trace element concentrations of selected phenocrysts determined by LA-ICP-MS analysis are discussed separately below.

Spinel

Chromian spinel and titanomagnetite are common accessory minerals in all samples from the back-arc mafic suite; the magnetite grains are most abundant in the groundmass and Cr-spinels occur mainly as inclusions in olivine. The latter are useful for calculations of temperature and oxygen fugacity based on chromite–melt and chromite–olivine equilibria described in the following section. Selected compositions of chromian spinels are reported in Table 5 and the full dataset is given in Supplementary Data Electronic Appendix 3.

Geothermobarometry

The magmatic conditions of P, T and oxygen fugacity (fO_2) have been estimated for 28 samples using a variety of calibrated mineral and mineral–melt equilibria, assuming that the host-rock compositions are close to those of the original melt. The results of the geothermometers and geobarometers applied are listed in Table 6, and a selection of preferred P–T results is shown in Fig. 10 based on data from phenocryst cores whose Fe–Mg partitioning (K_D) with the host-rock composition demonstrates a good approach to equilibrium (see below and Figs 7b and 9). The assumption that host-rock compositions are close to those of the original melt is reasonable considering the low abundance of phenocrysts in the samples and the positive test for equilibrium Mg–Fe partitioning. Devitrified groundmass glass was analysed by electron microprobe in some samples, but the glass data and phenocryst rims yielded K_D values far from Fe–Mg equilibrium so they are of no value for P–T calculations. The late contamination of some lavas by quartz-rich rocks has been mentioned above but its effect on mineral–melt geothermobarometry, if any, is avoided by the screening for equilibrium K_D partitioning.

Table 3: Composition of olivine phenocryst cores from the back-arc mafic suite

Sample:	SAF24	SAF32	SAF65	SAF71	SAF76	SAF200	SAF201	SAF202	SAF207	SAF208	SAF214	SAF218	SAF220	RP 1997
n:	7	5	4	5	15	8	10	6	20	5	18	5	20	4
SiO_2	39·90 (1·1)	39·69 (0·8)	38·67 (0·5)	39·34 (0·6)	39·68 (0·5)	39·42 (1·5)	39·86 (1·5)	39·65 (1·1)	40·34 (1·4)	39·92 (0·4)	39·81 (1·2)	39·28 (0·8)	40·16 (1·3)	39·27 (0·1)
FeO	11·88 (0·8)	14·72 (4·4)	15·74 (3·8)	15·00 (1·1)	15·13 (2·3)	16·81 (3·5)	12·65 (2·7)	14·82 (0·8)	12·21 (4·5)	13·22 (0·6)	13·68 (3·7)	14·18 (2·3)	11·96 (3·1)	13·13 (1·1)
MnO	0·19 (0·05)	0·17 (0·11)	0·16 (0·14)	0·21 (0·09)	0·23 (0·09)	0·21 (0·11)	0·21 (0·06)	0·20 (0·11)	0·17 (0·12)	0·17 (0·07)	0·24 (0·17)	0·14 (0·13)	0·18 (0·13)	0·19 (0·07)
MgO	47·96 (0·9)	46·16 (3·9)	45·34 (2·8)	45·22 (0·7)	45·35 (1·6)	44·15 (2·9)	47·02 (2·0)	45·87 (0·7)	48·09 (3·3)	46·73 (0·2)	46·46 (2·8)	46·14 (1·8)	47·67 (2·3)	48·03 (1·2)
NiO	0·31 (0·14)	0·28 (0·07)	0·34 (0·27)	0·28 (0·16)	0·33 (0·18)	0·36 (0·16)	0·34 (0·22)	0·35 (0·15)	0·63 (0·40)	0·40 (0·14)	0·30 (0·25)	0·26 (0·13)	0·44 (0·20)	0·32 (0·21)
CaO	0·17 (0·06)	0·12 (0·03)	0·13 (0·03)	0·13 (0·09)	0·14 (0·02)	0·12 (0·8)	0·13 (0·04)	0·10 (0·04)	0·09 (0·4)	0·13 (0·03)	0·10 (0·13)	0·12 (0·03)	0·13 (0·04)	0·10 (0·02)
Total	100·40	101·15	100·37	100·18	100·86	101·06	100·26	101·40	101·58	100·56	100·66	100·12	100·53	101·14
Fo	87·6 (0·9)	84·7 (5·1)	83·6 (4·3)	84·1 (1·2)	84·0 (2·5)	82·2 (4·1)	86·7 (3·0)	84·5 (0·9)	87·4 (4·9)	86·2 (0·6)	85·62 (4·0)	85·17 (2·6)	87·50 (3·3)	86·54 (1·3)

Sample:	RAN1	RAN2	RAN3	RAN4	RAN5a	RAN6	RAN7	RAN8a	RAN9	RAN10	RAN11b	RM568	RM810	CO99
Type:*	WP	WP	trans	WP	WP	trans	trans	WP	CA	CA	CA	WP	WP	WP
n:	7	16	5	11	12	6	10	4	16	9	11	44	3	5
SiO_2	40·32 (0·5)	40·13 (1·2)	39·55 (0·6)	39·53 (1·2)	40·15 (1·1)	39·72 (0·6)	38·67 (1·1)	39·15 (0·6)	39·03 (1·2)	39·78 (0·9)	38·98 (1·2)	39·5	39·8	39·58 (0·7)
FeO	11·52 (1·0)	11·15 (2·9)	14·99 (0·7)	15·89 (1·8)	11·01 (1·2)	12·19 (1·0)	12·34 (1·6)	14·81 (1·6)	11·90 (3·8)	13·38 (4·9)	12·87 (2·5)	16·7	15·3	12·22 (1·6)
MnO	0·14 (0·09)	0·15 (0·10)	0·22 (0·06)	0·24 (0·05)	0·12 (0·12)	0·23 (0·16)	0·21 (0·07)	0·25 (0·07)	0·17 (0·15)	0·18 (0·09)	0·16 (0·10)	0·22	0·16	0·19 (0·13)
MgO	48·40 (1·0)	48·20 (1·9)	45·14 (0·5)	45·01 (1·3)	48·18 (1·1)	47·59 (0·7)	47·44 (1·8)	45·86 (1·8)	47·43 (2·7)	46·62 (3·8)	46·59 (2·1)	44·6	45·9	47·37 (0·9)
NiO	0·31 (0·25)	0·35 (0·18)	0·31 (0·09)	0·27 (0·10)	0·39 (0·13)	0·40 (0·08)	0·45 (0·22)	0·31 (0·18)	0·38 (0·28)	0·46 (0·27)	0·37 (0·18)	0·18	0·23	0·31 (0·06)
CaO	0·09 (0·04)	0·11 (0·03)	0·11 (0·02)	0·15 (0·04)	0·13 (0·03)	0·16 (0·04)	0·13 (0·04)	0·14 (0·05)	0·10 (0·04)	0·11 (0·09)	0·14 (0·11)	0·13	0·11	0·13 (0·02)
Total	100·86	100·10	100·42	101·20	99·98	100·46	99·25	100·52	99·02	100·53	99·07	101·02	101·5	99·80
Fo	88·0 (1·1)	88·4 (3·1)	84·1 (0·8)	83·3 (1·9)	88·5 (1·3)	87·2 (1·0)	87·1 (1·8)	84·4 (3·7)	87·5 (4·2)	86·0 (5·5)	86·48 (2·8)	82	84	87·18 (1·6)

For each sample, olivine analysis listed was used in *P–T* calculations (Table 6). All data are given in Electronic Appendix 1. Values are in wt %; numbers in parentheses give the range of values (max–min). Fo is mol % forsterite component.

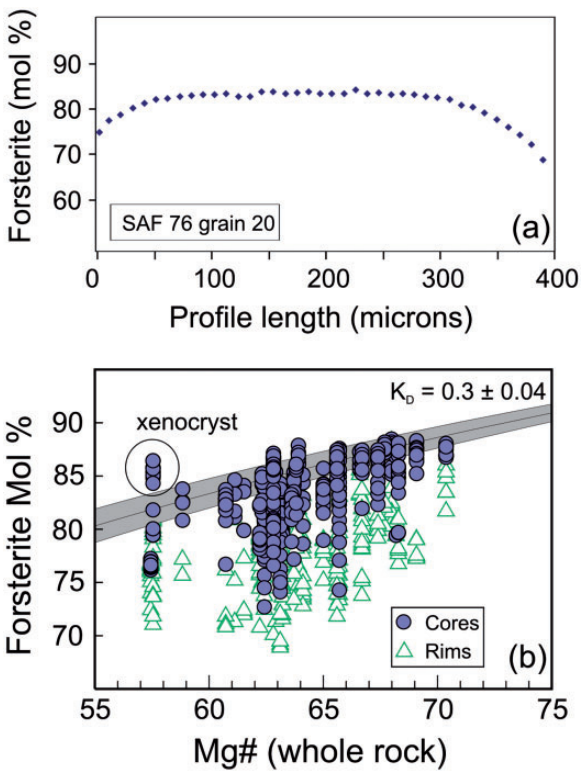

Fig. 7. (a) Representative zoning profile of olivine in sample SAF76; (b) comparison of olivine core and rim compositions with the host-rock Mg# [assuming $Fe^{3+}/(Fe^{2+}+Fe^{3+})=0{\cdot}1$]. The shaded band represents crystal–melt equilibrium for K_D (Fe–Mg) values of $0{\cdot}3 \pm 0{\cdot}04$.

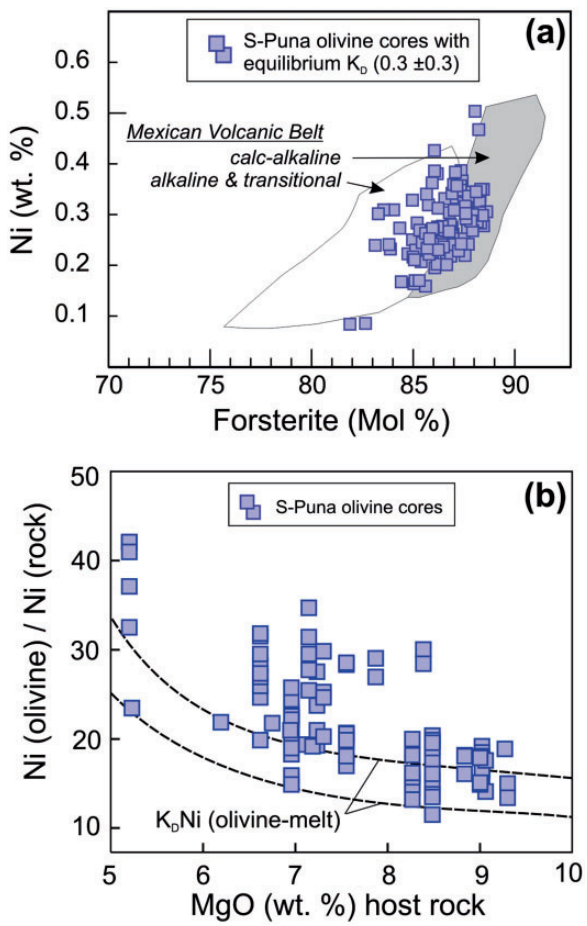

Fig. 8. Ni concentrations vs Fo mol % for olivine core compositions in the southern Puna mafic suite that satisfy the K_D (Fe–Mg) criteria of equilibrium with the host-rock ($0{\cdot}3 \pm 0{\cdot}04$). (a) NiO (wt %) plotted against mole per cent forsterite, with background fields from the Mexican Volcanic Belt for comparison (Straub *et al.*, 2008); (b) Ni in olivine/Ni in host-rock plotted against host-rock MgO. The dashed curves show the range of Mg-dependent olivine/melt Ni distribution coefficients compiled by Straub *et al.* (2008).

The olivine–melt temperatures calculated from three geothermometers (Table 6) agree within 50°C, which is close to the error estimates of ±30°C inherent in the calibrations (Putirka, 2008). In his overview of thermobarometry in basaltic systems, Putirka (2008) concluded that the olivine–melt thermometer of Beattie (1993) with a pressure term from Herzberg & O'Hara (2002) best reproduces anhydrous experimental data but overestimates temperatures for hydrous melts. The preferred temperature range for this thermometer (for samples with $K_D = 0{\cdot}26$–$0{\cdot}34$) is 1220–1322°C (Fig. 10a). The olivine–melt thermometer of Putirka (2008, equation 22) takes water into account, and for the whole-rock concentrations of 0·3–1·1 wt % H_2O (Table 1) it yielded temperatures 20–50°C lower than the Beattie–Herzberg–O'Hara values (Fig. 10b). The true water contents of the primary melts crystallizing olivine are unknown, but they are unlikely to be as high as the present bulk-rock values. Olivine-hosted melt inclusions in sample RAN2 (see below) in fact have lower water contents than the bulk-rock (<0·5 wt %, vs 0·89 wt %). Because of the uncertainty in primary water contents, we consider the anhydrous, pressure-corrected Beattie (1993) thermometer as the method of choice for this study, although noting that the temperature values would be up to 50°C lower if the melts were as hydrous as the bulk-rocks. Regardless of this detail, all thermometers suggest maximum crystallization temperatures above 1280°C, which is higher than the range of basaltic magmas in many terrestrial settings (compare Herzberg *et al.*, 2007; Putirka *et al.*, 2007; Lee *et al.*, 2009), and provides further evidence for elevated mantle temperature beneath the southern Puna plateau.

Clinopyroxene–melt equilibria are sensitive to both temperature and pressure. The results from several thermobarometry models are compared for the southern Puna samples in Table 6. The Putirka *et al.* (2003) model allows simultaneous solution for both P and T using iterative methods, and this yielded P estimates mostly in the range of 0·7–1 GPa. The temperatures from three thermometers

Table 4: Composition of clinopyroxene phenocryst cores from the back-arc mafic suite

Sample:	SAF71	SAF76	SAF200	SAGF201	SAF202	SAF207	SAF208	RP 1997	CO99
n:	2	20	6	6	6	6	9	27	31
SiO_2	52·49 (3·9)	53·69 (2·5)	52·17 (3·1)	52·39 (2·7)	50·60 (3·1)	52·31 (1·1)	51·56 (3·5)	52·29 (1·7)	52·85 (3·8)
TiO_2	0·66 (0·84)	0·40 (0·35)	0·47 (0·41)	0·43 (0·50)	0·99 (0·92)	0·72 (0·33)	0·79 (0·84)	0·33 (0·36)	0·39 (0·72)
Al_2O_3	2·57 (3·2)	2·29 (1·6)	1·50 (2·1)	2·48 (2·4)	3·89 (2·7)	2·86 (1·1)	2·92 (3·4)	2·72 (1·9)	2·55 (3·2)
FeO	6·44 (0·4)	5·96 (1·1)	7·19 (0·8)	7·10 (0·8)	6·83 (1·7)	6·31 (1·3)	7·05 (1·3)	4·42 (1·5)	5·64 (2·2)
MnO	0·11 (0·03)	0·20 (0·10)	0·16 (0·18)	0·31 (0·20)	0·13 (0·13)	0·16 (0·08)	0·19 (0·60)	0·20 (0·25)	0·25 (0·15)
MgO	16·73 (2·3)	18·32 (1·9)	17·89 (2·2)	17·37 (2·1)	15·54 (1·5)	16·29 (0·5)	16·30 (2·3)	16·86 (1·7)	18·10 (3·2)
CaO	21·17 (0·5)	19·01 (2·0)	19·83 (1·7)	19·06 (2·4)	21·44 (0·9)	21·99 (1·9)	21·16 (0·8)	21·02 (2·4)	18·98 (2·7)
Na_2O	0·29 (0·42)	0·37 (0·13)	0·23 (0·14)	0·22 (0·11)	0·30 (0·05)	0·25 (0·07)	0·31 (0·15)	0·46 (0·27)	0·37 (0·20)
Cr_2O	0·51 (0·78)	0·76 (0·53)	0·30 (0·29)	0·26 (0·47)	0·47 (0·42)	0·48 (0·30)	0·30 (0·22)	0·59 (0·98)	0·55 (0·76)
Total	100·36	101·01	100·65	99·60	100·26	101·37	100·59	98·89	99·68
Wo	41·80 (3·2)	38·55 (4·4)	42·72 (4·8)	38·88 (6·0)	44·21 (1·2)	44·25 (3·0)	42·75 (3·6)	43·72 (5·6)	38·92 (5·8)
En	46·86 (4·5)	51·70 (4·9)	46·97 (4·7)	49·31 (4·9)	44·56 (2·8)	45·59 (1·4)	45·83 (4·5)	48·80 (3·8)	51·65 (7·5)
Fs	11·34 (1·4)	9·75 (1·9)	10·31 (1·2)	11·80 (1·6)	11·21 (3·0)	10·16 (2·2)	11·42 (2·5)	7·50 (2·4)	9·43 (4·1)

Sample:	RAN1	RAN3	RAN5b	RAN6	RAN9	RAN10	RAN11b	RM810	RM568
n:	4	4	4	10	4	14	22	5	7
SiO_2	53·39 (2·4)	51·55 (3·2)	51·50 (1·7)	51·58 (4·7)	53·23 (1·5)	52·84 (3·6)	52·41 (4·2)	50·98 (1·4)	52·75 (4·6)
TiO_2	0·33 (0·43)	0·76 (0·46)	0·69 (0·36)	0·61 (1·30)	0·34 (0·20)	0·30 (0·98)	0·44 (0·97)	0·98 (0·57)	0·37 (1·10)
Al_2O_3	1·43 (2·2)	2·51 (2·5)	2·39 (1·5)	2·46 (4·6)	2·29 (1·1)	1·97 (2·7)	2·17 (3·5)	4·44 (1·0)	1·62 (4·2)
FeO	5·83 (0·8)	6·91 (0·9)	6·62 (0·6)	6·78 (1·8)	4·70 (1·4)	6·01 (2·4)	6·71 (1·5)	7·23 (1·3)	8·17 (1·4)
MnO	0·18 (0·11)	0·12 (0·03)	0·15 (0·20)	0·15 (0·23)	0·11 (0·08)	0·17 (0·20)	0·20 (0·09)	0·20 (0·12)	0·22 (0·10)
MgO	18·21 (2·2)	16·61 (1·8)	17·20 (2·0)	17·44 (3·7)	17·20 (0·5)	18·74 (3·3)	17·86 (3·2)	15·28 (1·4)	17·27 (3·2)
CaO	19·95 (1·0)	20·16 (1·0)	20·31 (1·2)	19·84 (2·2)	21·85 (1·7)	18·57 (3·2)	18·96 (2·8)	21·34 (3·0)	18·08 (3·6)
Na_2O	0·21 (0·11)	0·25 (0·12)	0·23 (0·08)	0·21 (0·17)	0·39 (0·16)	0·44 (0·19)	0·25 (0·16)	0·34 (0·07)	0·42 (0·24)
Cr_2O	0·38 (0·34)	0·11 (0·53)	0·20 (0·13)	0·35 (0·70)	0·52 (0·31)	0·55 (0·73)	0·41 (0·38)	0·37 (0·32)	0·05 (0·25)
Total	99·89	99·01	99·28	99·42	100·66	99·58	99·40	101·16	99·12
Wo	39·92 (3·4)	41·34 (3·6)	41·00 (3·5)	40·06 (6·2)	44·12 (2·5)	37·54 (7·3)	38·54 (6·9)	44·09 (6·2)	37·15 (8·4)
En	50·70 (4·7)	47·39 (3·5)	48·32 (4·6)	49·00 (7·7)	48·30 (1·3)	52·72 (8·2)	50·50 (7·3)	43·93 (4·1)	49·38 (8·1)
Fs	9·39 (1·6)	11·26 (1·4)	10·68 (1·0)	10·94 (3·2)	7·58 (2·4)	9·74 (4·5)	10·96 (2·7)	11·98 (2·4)	13·46 (2·8)

Each sample gives the analysis used in *P–T* calculations. All data are given in Electronic Appendix 2. Values are from electron microprobe in wt %, numbers in parentheses give the range (max–min). Wo, En and Fs are mol % wollastonite, enstatite and ferrosilite components, respectively. RAN5a and RAN5b are samples from the same flow.

requiring a fixed pressure estimate [COMAGMAT of Ariskin *et al.* (1993), and equations (32d) and (34) from Putirka (2008)] were calculated for 1 GPa accordingly. The results of all pyroxene geothermometers are similar. COMAGMAT consistently yielded temperatures *c.* 60–80° higher than the other three, which among themselves agree within the 30°C calibration uncertainty (Putirka, 2008). The range of preferred temperature estimates from samples with near-equilibrium compositions ($K_D = 0{\cdot}2$–$0{\cdot}4$) is 1230–1140°C (Fig. 10c), which is *c.* 100°C lower than the olivine crystallization range (Fig. 10a and b). This difference is beyond the uncertainty of the methods and suggests that olivine crystallized before clinopyroxene. As noted above, the order of crystallization of the two phenocryst phases is not clear from the petrography (Fig. 3), but the observation that some samples contain only olivine phenocrysts supports an earlier crystallization of that phase. Model calculations of the crystallization sequence for the bulk-rock compositions using the Pele software (Boudreau, 1999) confirm that olivine is the expected liquidus phase for crystallization pressures of 0·5–1 GPa.

The pressure estimates from four clinopyroxene–melt geobarometers from Putirka (2008) are compared in

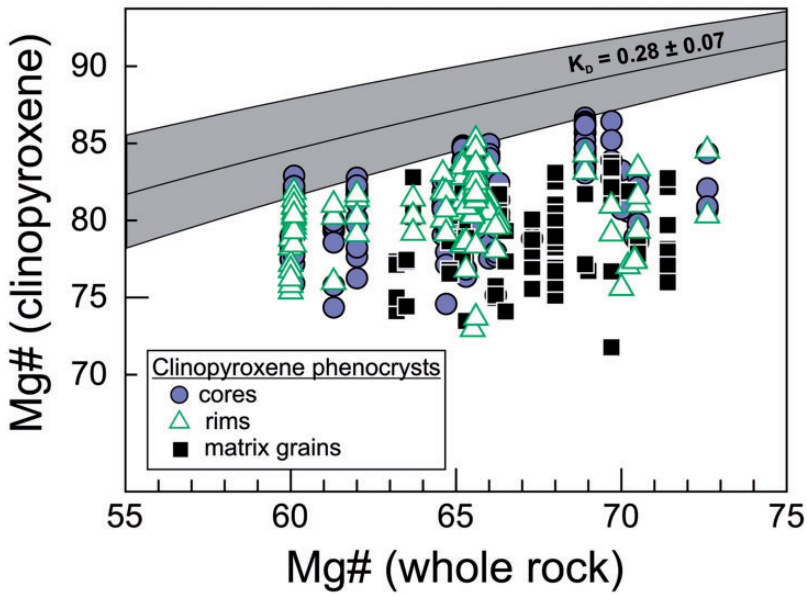

Fig. 9. Comparison of clinopyroxene phenocryst (core and rim) and matrix grain compositions with the host-rock Mg# [assuming whole-rock $Fe^{3+}/(Fe^{2+}+Fe^{3+}) = 0{\cdot}1$]. The shaded band represents crystal–melt equilibrium for K_D (Fe–Mg) values of $0{\cdot}28 \pm 0{\cdot}07$.

Table 6 along with an independent estimate based on the pressure dependence of silica activity in primary melts. Three of the four clinopyroxene–melt geobarometers yield pressure estimates in the range of 0·5–1·0 GPa (only near-equilbrium samples with $K_D = 0{\cdot}2$–$0{\cdot}4$; see Fig. 10c). The fourth [equation (30) of Putirka (2008)] gives consistently lower estimates (0·4–0·5 GPa). We prefer the higher pressure estimates because two of the geobarometers in this range are based on different exchange reactions (Ca–Na- and Al-tchermakite). Also, the silica activity barometer yields pressures in the high range (Table 6). There is a possible bias in this method owing to excess SiO_2 from late crustal contamination in some lavas. That effect would be to underestimate the pressure (by 1·5 kbar for 2 wt % excess SiO_2), so the values in Table 6 are considered as minima. Figure 10c shows the clinopyroxene–melt pressure and temperature values from simultaneous solution of the Putirka *et al.* (2003) calibrations. It should be noted that P and T are strongly correlated on this plot, but that relates to the functional relationships of the two variables in the thermobarometry equations and does not necessarily have geological significance.

The olivine–spinel exchange thermometer of Poustovetov (2000) returns much lower equilibrium temperatures than olivine–melt or clinopyroxene–melt. The results for olivine core compositions and spinel inclusions in them yield temperatures of 1083–850°C (Table 6). We attribute the lower temperatures to continued Mg–Fe exchange between olivine and spinel during cooling (see also Clyne & Borg, 1997). Estimates of oxygen fugacity from spinel–melt equilibrium (using bulk-rock compositions) after Poustovetov & Roeder (2000) yield log fO_2 values between −7·6 and −10·0 for 14 of the 18 samples where the method could be applied. This range corresponds to between zero and 2·4 log units below the quartz–fayalite–magnetite (QFM) buffer at 1200°C and 1 GPa.

TRACE ELEMENTS IN CLINOPYROXENE

The *in situ* trace element analyses of clinopyroxene phenocrysts allow compositional information on parental melts to be linked with the pressure–temperature estimates and mark specific stage(s) of magma evolution with ascent and cooling. The pyroxenes chosen for LA-ICP-MS analysis are from six relatively primitive samples (bulk-rock $SiO_2 = 50{\cdot}8$–$54{\cdot}5$ wt %; Mg# = 77–87; mostly of the CA type). Multiple grains were analyzed in each sample at unaltered, inclusion-free sites. Average values are reported in Table 7 and the full dataset is given in Supplementary Data Electronic Appendix 4. Typical within-sample variations in trace element concentrations are less than 25% relative to the reported average, and correlations of trace element contents with the Mg# of the pyroxene (not shown) suggest that much of the variation reflects pyroxene growth during magmatic differentiation. One very important feature of the clinopyroxene trace element compositions is that all samples show a negative Eu anomaly (Eu/Eu* = 0·77–0·88; see Fig. 11a). As discussed above, negative Eu anomalies in the plagioclase phenocryst-free whole-rocks are evidence for crustal assimilation. Finding Eu anomalies in clinopyroxene means that assimilation took place before or during crystallization of that mineral.

Table 5: Composition of chromian spinel from the back-arc mafic suite

Sample:	SAF76		SAF201		SAF202		SAF207		SAF208		SAF214		SAF218		SAF220		RP 1997		CO99	
n:	3	*r*	7	*r*	6	*r*	13	*r*	4	*r*	14	*r*	9	*r*	28	*r*	3	*r*	6	*r*
TiO_2	1·68	0·2	0·89	0·2	1·42	0·6	1·09	0·6	1·40	0·03	1·40	0·7	1·34	0·6	0·91	1·3	1·00	0·1	0·86	0·1
Al_2O_3	17·27	0·6	21·01	3·2	19·56	3·5	14·05	3·4	16·04	0·8	17·52	2·9	18·61	2·8	24·88	7·6	21·11	0·4	25·58	2·0
Cr_2O_3	37·22	0·3	38·03	1·9	35·63	1·5	46·34	3·8	41·25	1·4	41·07	3·9	34·47	4·1	35·16	3·9	37·50	0·8	34·91	2·0
Fe_2O_3	13·96	0·9	10·12	3·0	12·47	2·9	9·12	5·5	10·98	1·2	10·06	3·6	14·16	5·0	9·40	7·9	11·30	0·8	9·39	1·9
FeO	21·11	0·6	16·50	3·9	18·75	2·7	17·18	3·7	18·74	0·6	18·04	3·5	19·54	2·6	15·05	4·4	18·00	1·7	15·53	1·9
MnO	0·19	0·02	0·20	0·2	0·18	0·1	0·10	0·1	0·17	0·1	0·14	0·2	0·29	0·1	0·15	0·2	0·20	0·04	0·11	0·1
MgO	9·83	0·4	12·31	3·1	11·16	2·0	11·44	2·5	10·69	0·4	11·55	2·4	10·23	2·3	13·79	2·7	11·77	1·3	13·73	1·1
NiO	0·13	0·04	0·36	0·3	0·21	0·2	0·38	0·2	0·29	0·1	0·17	0·3	0·19	0·2	0·25	0·3	0·24	0·1	0·27	0·05
ZnO	0·24	0·2	0·13	0·2	0·0	0·2	0·12	0·2	0·18	0·2	0·03	0·3	0·16	0·2	0·15	0·4	0·18	0·1	0·06	0·1
Total	101·67		99·62		99·49		99·93		99·80		100·06		99·07		99·82		101·35		100·51	
Cr#	0·49		0·48		0·46		0·61		0·55		0·54		0·46		0·43		0·47		0·43	
Al#	0·34		0·40		0·38		0·28		0·32		0·34		0·37		0·46		0·39		0·47	
Fe#	0·17		0·12		0·15		0·11		0·14		0·12		0·18		0·11		0·13		0·11	

Sample:	RAN1		RAN2		RAN3		RAN4		RAN5a		RAN6		RAN7		RAN8a		RAN9	
n:	7	*r*	10	*r*	4	*r*	11	*r*	10	*r*	4	*r*	7	*r*	3	*r*	5	*r*
TiO_2	0·77	0·2	0·80	0·4	1·95	0·5	2·55	1·3	0·90	0·3	0·83	0·2	1·21	0·5	1·41	0·2	1·00	0·1
Al_2O_3	16·13	3·3	16·94	3·6	19·08	1·1	20·51	5·1	26·58	3·2	23·70	2·2	22·89	3·0	23·68	0·5	20·36	1·2
Cr_2O_3	44·59	4·3	43·98	3·9	32·55	1·6	30·86	2·3	34·18	2·2	35·02	2·3	34·36	3·7	32·39	0·4	34·26	1·8
Fe_2O_3	9·53	0·9	9·35	4·0	13·94	2·2	15·71	4·1	9·49	3·3	10·22	0·9	11·08	3·6	12·50	0·5	13·72	1·1
FeO	15·54	1·3	15·73	2·3	18·39	2·1	19·48	2·7	13·62	3·3	14·82	0·8	16·02	2·2	17·94	0·7	18·97	0·9
MnO	0·15	0·1	0·15	0·1	0·15	0·1	0·21	0·1	0·07	0·2	0·07	0·2	0·17	0·1	0·19	0·03	0·18	0·1
MgO	12·48	0·7	12·53	1·7	11·15	1·2	11·69	1·5	15·09	2·5	13·66	0·6	12·98	1·7	12·29	0·2	10·82	1·7
NiO	0·23	0·1	0·18	0·2	0·27	0·1	0·19	0·1	0·31	0·3	0·20	0·2	0·32	0·2	0·24	0·1	0·22	0·1
ZnO	0·12	0·2	0·16	0·2	0·11	0·1	0·12	0·1	0·12	0·1	0·10	0·2	0·08	0·1	0·03	0·2	0·20	0·2
Total	99·62		99·92		97·69		101·37		100·45		98·74		99·21		100·77		99·90	
Cr#	0·57		0·56		0·44		0·40		0·41		0·44		0·43		0·41		0·44	
Al#	0·31		0·32		0·38		0·40		0·48		0·44		0·43		0·44		0·39	
Fe#	0·12		0·11		0·18		0·20		0·11		0·12		0·13		0·15		0·17	

Values given for representative analysis of spinel inclusions in olivine used for T–fO_2 estimates. Also shown are number of grains analysed (*n*) and range of values (*r*). Analyses by electron microprobe (in wt %), Fe^{2+} and Fe^{3+} distribution was calculated following Droop (1987). $Cr\# = 100Cr/(Fe^{3+} + Cr + Al)$, $Al\# = 100Al/(Fe^{3+} + Cr + Al)$, $Fe\# = 100Fe^{3+}/(Fe^{3+} + Cr + Al)$.

Based on the 0·7–1 GPa pressure estimates for clinopyroxene crystallization, the assimilation took place at or below 20–35 km depth in the crust.

The ratio of element concentrations in clinopyroxene to those of the respective host-rock can be regarded as an empirical mineral–melt distribution coefficient for that element, and these ratios are tested for agreement with experimental *D* values for clinopyroxene in basaltic systems from White (2009, table 7.05) in Fig. 11b. The agreement is within a factor of two (shaded field) for all elements except for a small group (Rb, Ba, Th, U, Nb), whose empirical *D* values are 5–10 times lower than the published range. Given the good agreement shown between empirical and published *D* values for the other trace elements, it seems unlikely that the published values are 'wrong' for this element group. Indeed, the same patterns of good (shaded band) vs poorer agreement shown in Fig. 11b also result if other compilations of clinopyroxene *D* values are used (Bedard, 1994; Dorais & Tubrett, 2008). Therefore, the explanation for mismatch between empirical and published *D* values for Rb, Ba, Th, U and Nb must be related to the samples. Either the measured

Table 6: Summary results of pressure–temperature calculations

Sample	Locality	Mineral-melt K_D		Ol saturation T		Olivine-melt T		Cpx saturation T		Cpx-melt T		Cpx-melt P				Si activity	Spinel-melt	
		(cpx)	(ol)	P(08) eq. 15	COMAG MAT	Beattie	P(08) eq. 22	COMAG MAT	RiM eq. 34	P(03)	P(08) eq. 32d	P(03)	P(08) eq. 30	P(08) eq. 31	P(08) eq. 32c	P(08) eq. 42	*T	†log fO_2
RAN1	La Falda	0·43	0·32	1274	1321	1322	1286	1282	1231	1221	1243	0·82	0·28	0·80	0·83	0·71	1067	−9·1
RAN2	La Falda		0·29	1264	1311	1316	1272										1070	−8·8
SAF65	Anto./Laguna		0·31	1231	1239	1263	1241											
RAN3	Anto./Laguna	0·35	0·32	1217	1243	1266	1227	1246	1184	1166	1206	0·67	0·20	0·73	0·72	0·62	1059	−5·3
RAN4	Antofalla		0·31	1220	1243	1268	1229										1083	−8·7
RAN5a	El Jote	0·46	0·27	1267	1301	1311	1273	1269	1218	1197	1215	0·73	0·19	0·68	0·86	1·06	1042	−8·0
SAF218	El Jote		0·31	1233	1252	1275	1240										940	−11·4
RAN6	El Jote	0·41	0·28	1262	1291	1306	1269	1268	1218	1205	1220	0·74	0·25	0·72	0·88	1·01	1056	−8·1
RAN7	El Jote		0·29	1258	1292	1306	1262										1016	−9·0
SAF220	El Jote		0·27	1250	1279	1296	1256										1002	−8·4
RAN8a	Carachi		0·30	1225	1241	1268	1230										1048	−10·0
SAF71	Carachi	0·44	0·35	1268	1276	1302	1286	1258	1235	1196	1221	0·86	0·27	0·78	0·76	1·02		
SAF200	Nacimientos	0·35	0·35	1191	1217	1242	1205	1244	1168	1162	1205	0·65	0·26	0·87	0·80	0·09		
SAF201	Nacimientos	0·41	0·27	1232	1246	1269	1226	1256	1190	1192	1217	0·63	0·24	0·75	0·72	0·57	997	−9·2
SAF202	Nacimientos	0·41	0·30	1218	1237	1262	1225	1251	1200	1190	1198	0·76	0·36	0·97	0·97	0·51	1024	−8·9
RAN10	Nacimientos	0·32	0·28	1210	1227	1251	1209	1260	1181	1203	1222	0·59	0·46	0·73	0·77	0·70	1083	−9·1
RAN11b	Nacimientos	0·29	0·21	1169	1184	1220	1159	1232	1137	1143	1206	0·46	0·18	0·66	0·60	0·17		
RM568	Vega Colorado	0·38	0·28	1205	1216	1244	1218	1238	1205	1181	1232	0·87	0·42	0·90	0·63	0·24		
SAF24	Diablo		0·27	1256	1270	1288	1261											
SAF32	Diablo		0·28	1230	1224	1254	1232											
SAF207	S Beltran	0·47	0·31	1232	1290	1294	1242	1265	1207	1193	1218	0·89	0·32	1·04	1·02	0·24	1041	−9·1
SAF208	S Beltran	0·43	0·28	1223	1245	1265	1231	1253	1202	1187	1205	0·75	0·33	0·89	0·89	0·48	981	−6·0
RAN9	Pasto Ventura	0·32	0·29	1271	1297	1313	1278	1272	1251	1226	1249	1·01	0·59	0·97	0·88	1·29	851	−6·8
RP1997	Pasto Ventura	0·29	0·31	1258	1274	1293	1265	1267	1249	1225	1255	1·01	0·66	1·02	0·89	1·18	940	−7·6
SAF76	Purulla	0·31	0·32	1219	1236	1264	1231	1250	1206	1197	1249	0·87	0·49	0·93	0·81	0·53		
CO99	S Antofalla	0·30	0·24	1217	1235	1260	1215	1251	1197	1194	1240	0·75	0·48	0·82	0·75	0·84		
SAF214	Hom-Muerto		0·28	1201	1226	1252	1205										1041	−10·0
RM810	Hom-Muerto	0·45	0·29	1220	1229	1251	1227	1252	1201	1188	1194	0·71	0·34	0·96	0·95	0·37		

All temperatures in °C, pressures in GPa. (See text for description of thermometers and barometers listed.) P(03), Putirka *et al.* (2003); P(08), Putirka (2008).
*Temperature from olivine–spinel equilibria, from Poustovetov (2000).
†Oxygen fugacity from spinel–melt equilibria, from Poustovetov & Roeder (2000).

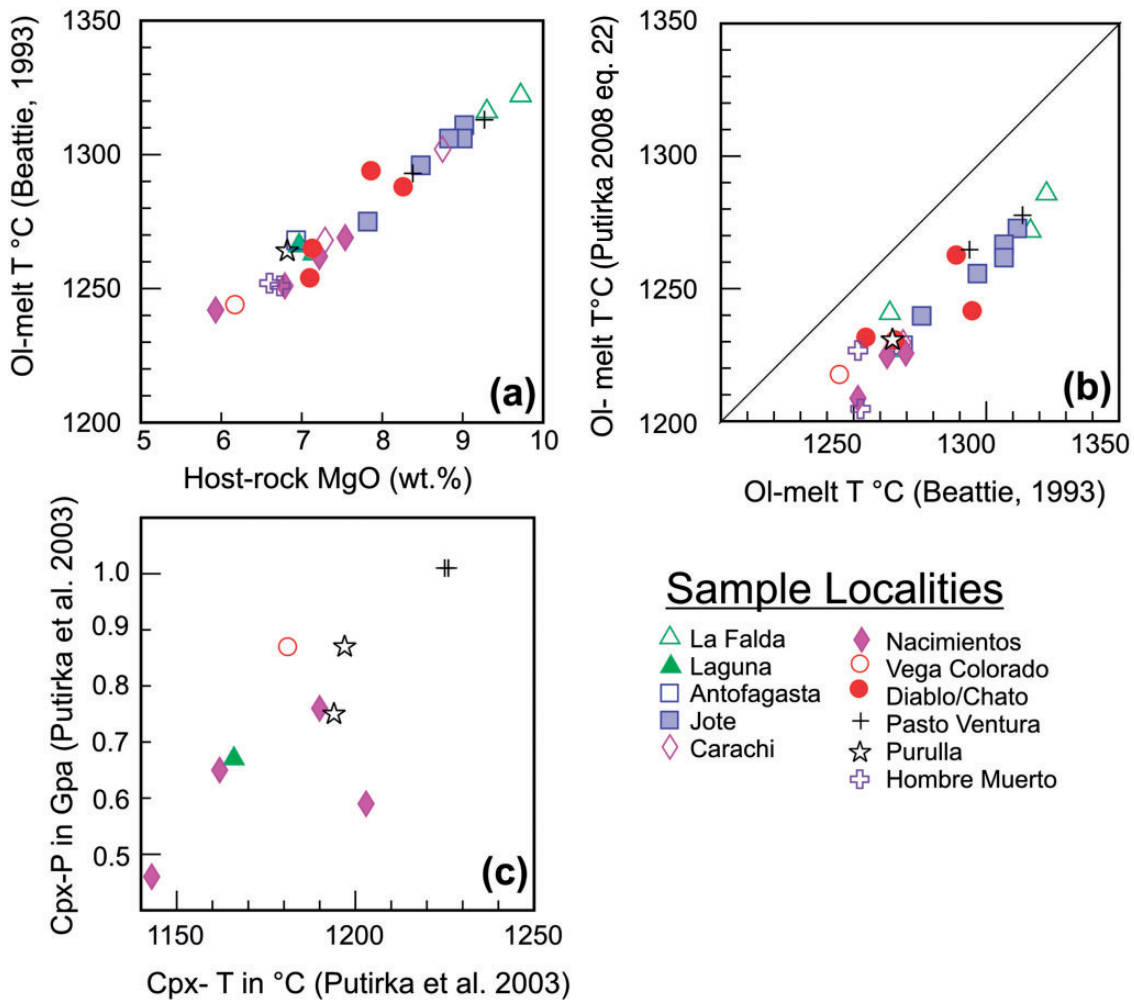

Fig. 10. Temperature and pressure estimates from olivine and clinopyroxene–melt equilibria. Points are plotted only for near-equilibrium mineral–melt pairs yielding K_D (Fe–Mg) of 0·26–0·34 for olivine, and 0·2–0·4 for clinopyroxene (see Table 6). (a) Olivine–melt temperatures for assumed anhydrous conditions (Beattie thermometer in Table 6) vs host-rock MgO; (b) shows the offset of 20–50°C between the values of Beattie (anhydrous) and Putirka [2008, equation (22) using whole-rock H_2O thermometers]; (c) results for simultaneous solution of clinopyroxene–melt equilbria for *P* and *T*. It should be noted that all localities have similar *P*–*T* ranges.

concentrations of these elements in clinopyroxene are too low or their concentrations in the whole-rocks are higher than in the melts from which clinopyroxene crystallized. It must be said that for some elements in this group, particularly Rb, the concentrations in clinopyroxene are at or near the detection limit in some samples (Table 7 and Electronic Appendix 4), and should be interpreted with caution. However, a reasonable explanation for the mismatch of empirical and published *D* values is that the concentrations of these elements in the whole-rocks are higher than in the melts from which clinopyroxene crystallized because of a later stage of assimilation.

We illustrate this in more detail by comparing the predicted trace element concentrations of model melts based on the clinopyroxene data and published *D* values with the whole-rock compositions. Plots for Th, U, Nb, La and Ta (Fig. 12) demonstrate that host-rocks and model melts have the same range of La and Ta concentrations (i.e. empirical and published *D* values agree), whereas the whole-rocks have higher concentrations than the model melts for Th, U and Nb. Qualitatively, the same is true for Rb and Ba (see Fig. 11) but these are not plotted in Fig. 12 because of uncertainty in the model melt compositions. For Rb, the problem is the very low Rb concentration in clinopyroxene (Table 7). For Ba, the uncertainty is in the clinopyroxene–melt *D* values. Even a conservative choice of D_{Ba} values from the GERM compilation (http://earthref.org/GERM/), taking only experimental results for tholeiitic basalt compositions and for publication dates after 2000, gives a range from 0·0002 to 0·005. That range yields Ba concentrations in model melts around 300 ppm or 15 ppm, respectively, which compare with *c.* 400 ppm in

Table 7: Trace element composition of clinopyroxene from the back-arc mafic suite

Sample:	RP 1997	SAF76	CO99	RAN1	SAF208	SAF201
n:	15	13	15	6	34	8
Sc	87 (7·4)	90 (5·2)	101 (11)	108 (17)	110 (10·2)	117 (8·6)
Cr	4604 (2756)	3488 (777)	4518 (1191)	1714 (710)	1349 (525)	2133 (581)
Ni	170 (45)	170 (17)	217 (89)	57 (12)	87 (9)	74 (19)
Rb[1]	0·06 (0·02, $n=2$)	0·08 (0·01, $n=2$)	0·06 ($n=1$)	0·03 (0·03, $n=2$)	0·05 (0·05, $n=20$)	0·01 (0·1, $n=4$)
Sr	103 (7)	52 (1·3)	47 (4·6)	43 (6·2)	39 (2·9)	27 (2·0)
Ba[1]	0·09 (0·03)	0·06 (0·02)	0·07 (0·04)	0·05 (0·02, $n=5$)	0·3 (0·39)	0·05 (0·02)
Y	13·6 (2·1)	15·2 (1·4)	17·7 (3·4)	18·7 (3·9)	17·8 (2·2)	15·6 (1·3)
Zr	22 (4·5)	19·3 (3·0)	27·4 (7·5)	23·7 (10·7)	28·3 (9·1)	17·4 (1·5)
Hf	1·0 (0·2)	0·86 (0·17)	1·29 (0·40)	1·1 (0·54)	1·33 (0·42)	0·85 (0·08)
Nb	0·07 (0·02)	0·06 (0·02)	0·11 (0·04)	0·07 (0·05)	0·06 (0·03)	0·02 (0·003)
Ta[1]	0·01 (0·003, $n=14$)	0·01 (0·03, $n=8$)	0·03 (0·01, $n=13$)	0·03 (0·01, $n=4$)	0·02 (0·01, $n=14$)	0·02 ($n=1$)
Th	0·05 (0·01)	0·03 (0·01)	0·03 (0·02)	0·03 (0·01)	0·03 (0·02)	0·02 (0·004)
U[1]	0·01 (0·003, $n=10$)	0·01 (0·03, $n=10$)	0·01 (0·001, $n=11$)	0·01 (0·002, $n=4$)	0·01 (0·002, $n=33$)	0·003 (0·001)
La	3·8 (0·62)	2·91 (0·22)	2·16 (0·53)	2·25 (0·73)	2·32 (0·53)	1·42 (0·08)
Ce	13·1 (2·1)	10·3 (0·7)	7·9 (1·9)	9·4 (2·9)	10·5 (2·3)	6·3 (0·22)
Pr	2·53 (0·4)	1·99 (0·15)	1·63 (0·38)	1·90 (0·57)	2·05 (0·41)	1·30 (0·06)
Nd	14·3 (2·2)	11·3 (0·8)	9·8 (2·2)	10·8 (3·1)	11·6 (2·16)	7·5 (0·46)
Sm	3·91 (0·54)	3·39 (0·29)	3·3 (0·72)	3·44 (0·95)	3·74 (0·62)	2·62 (0·18)
Eu	1·09 (0·14)	0·89 (0·07)	0·94 (0·19)	0·98 (0·26)	1·02 (0·17)	0·73 (0·06)
Gd	3·64 (0·52)	3·62 (0·37)	3·72 (0·76)	3·86 (0·94)	4·08 (0·57)	3·16 (0·25)
Tb	0·51 (0·07)	0·53 (0·05)	0·59 (0·12)	0·59 (0·15)	0·60 (0·08)	0·50 (0·04)
Dy	3·06 (0·43)	3·30 (0·27)	3·85 (0·80)	4·05 (0·93)	3·99 (0·53)	3·36 (0·28)
Ho	0·54 (0·08)	0·62 (0·06)	0·70 (0·14)	0·78 (0·17)	0·71 (0·09)	0·63 (0·06)
Er	1·35 (0·21)	1·58 (0·16)	1·82 (0·36)	2·02 (0·06)	1·79 (0·23)	1·62 (0·14)
Tm	0·17 (0·03)	0·21 (0·02)	0·24 (0·05)	0·27 (0·06)	0·23 (0·03)	0·21 (0·02)
Yb	1·04 (0·19)	1·33 (0·15)	1·49 (0·31)	1·70 (0·38)	1·41 (0·19)	1·31 (0·12)
Lu	0·14 (0·02)	0·18 (0·02)	0·20 (0·04)	0·24 (0·05)	0·19 (0·03)	0·18 (0·02)
Eu_N/Eu^*	0·88 (0·02)	0·77 (0·03)	0·82 (0·03)	0·83 (0·03)	0·80 (0·02)	0·78 (0·02)

Trace elements in ppm by LA-ICP-MS, values are average of *n* points, numbers in parentheses give one standard deviation. $Eu^* = (Sm_N \times Gd_N)^{0.5}$.
[1]Concentrations at some points are below detection limit; mean and range are based on $n = x$ values.

the whole-rocks (Table 1). We believe that the lower range is more reasonable because values of D_{Ba} greater than 0·001 predict Ba enrichment of whole-rocks vs model melts by a factor of five and more, whereas all reasonable crustal contaminants (basement rocks, felsic melts) have double the Ba concentration of the whole-rocks at most.

Figure 12 shows that the relevant compositions of components in the upper crust in the region could be considered in an assimilation scenario [e.g. Paleozoic granitic rocks from Lucassen *et al.* (2001); Pliocene Cerro Galán ignimbrites and glassy dacite from Kay *et al.* (2010)]. There are several reasons why mixing with Pliocene silicic magma is a more likely scenario than assimilation of Paleozoic granitic rocks. First, the U and Th concentrations in the volcanic units are higher and less assimilation is required (see below). Second, magma mixing is much more efficient energetically than assimilation of basement rocks in the upper crust. Third and most compelling, there is an abundance of silicic lava and ignimbrites with similar ages and location in the southern Puna to the mafic lavas. Kay *et al.* (2011) argued that the silicic magmas erupted at Cerro Galán collected in a crystal mush zone at about 20 km depth before segregating and ascending into the shallow sub-caldera magma chambers. A partially molten mush zone would be a favorable site for interaction of ascending mafic magmas with felsic melts. Simple mixing models for sample SAF208 to test the idea of crustal assimilation (Fig. 13) show that about 20%

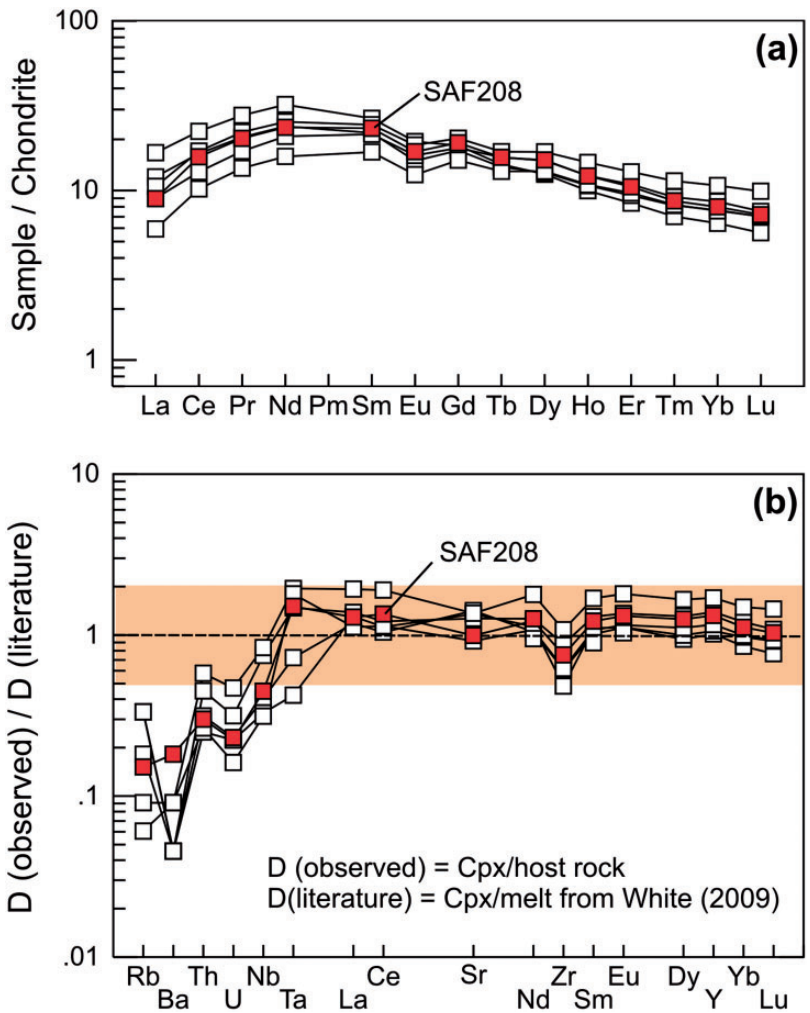

Fig. 11. (a) Chondrite-normalized (Sun & McDonough, 1989) REE contents in clinopyroxenes determined by LA-ICP-MS analysis. Sample 208 is highlighted because of its use in the model melt calculations. (b) Comparison of observed trace element distribution coefficients (mineral/host-rock ratio) for mafic suite samples with literature clinopyroxene–basalt *D* values from White (2009). The shaded band represents a 200% range centered on the literature *D* values. The observed *D* values plot within this shaded envelope for all but a small group of highly incompatible elements, which is attributed to the effect of additional crustal assimilation by the magma after Cpx crystallization (see text).

addition of glassy dacite SAF44 to the model melt composition explains most of the trace element features of the bulk-rock (Fig. 13a). It should be noted that the same model using the Galán ignimbrite composition (Fig. 13b) provides a poorer fit.

To summarize the significance of clinopyroxene trace element variations, the presence of negative Eu anomalies in clinopyroxene requires that these features were present in the ambient melts at the time of crystallization. The agreement of empirical and published *D* values for many other trace elements (e.g. REE, Sr, Zr, Ta) indicates that the melts crystallizing pyroxene had a similar composition to the erupted lavas. In contrast, there is a strong mismatch of empirical and published *D* values for highly incompatible elements enriched in the crust (Rb, Ba, Th, U, Nb), suggesting additional assimilation after clinopyroxene crystallization, and thus at depths shallower than 20–35 km. The most likely scenario for this assimilation, from both geological and geochemical arguments, is mixing in the upper crust with contemporary silicic magmas.

MELT INCLUSIONS

Olivine-hosted melt inclusions are present in several samples from the mafic suite but they are generally too few and too small (<10 μm across) for meaningful analysis. The exception to this is sample RAN2, whose olivine phenocrysts have relatively abundant and large primary melt inclusions (Fig. 14). The host olivine grains in RAN2 have compositions varying from Fo_{86} to Fo_{89} with narrow, more Fe-rich rims (<20 μm) of $Fo_{76–79}$. This sample belongs

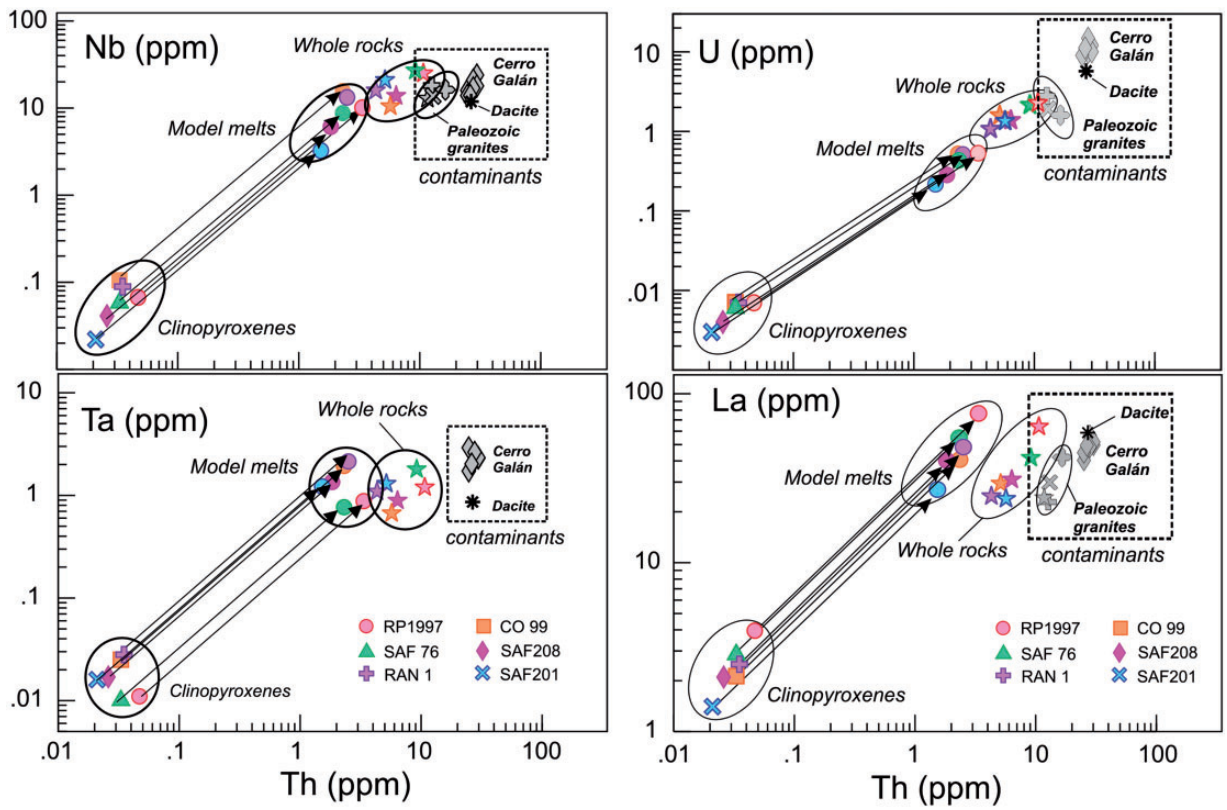

Fig. 12. Comparison of Nb, Ta, U, Th and La concentrations in clinopyroxene with hypothetical model melts calculated using the Cpx–melt *D* values of White (2009). The model melts match the observed whole-rocks for La and Ta, but are deficient in Nb and strongly so for U and Th (compare Fig. 1b). Possible crustal contaminants that can explain the offset between the model melts and whole-rock compositions are highlighted (see text for data sources).

to the within-plate (WP) compositional group and is one of the most primitive samples in the suite, with 9·3 wt % MgO and 484 ppm Cr. The primary melt inclusions in sample RAN2 are typically glassy and colorless to light yellow–green. Less common are devitrified inclusions with a darker, brownish hue. Inclusions are spherical to ellipsoidal, of 5–90 μm diameter (mostly <60 μm). At room temperature, the inclusions contain a vapor bubble that occupies 5–10% of their volume. The glassy inclusions were exposed by polishing and were analyzed directly by electron microprobe. The devitrified melt inclusions contain microcrystals of clinopyroxene, spinel and rare sulfides. These inclusions were re-homogenized to glass on a microscope heating stage (see 'Sample distribution and analytical methods'). Homogenization runs at 1150–1250°C succeeded in melting the silicate phases in the inclusions, but not uncommonly a chrome-spinel crystal remained within the inclusion volume, which we interpret as a solid inclusion trapped with the melt (Fig. 14). The vapor bubbles never completely disappeared in heating runs, probably because of the much lower pressure relative to the original trapping conditions (Tait, 1992).

One motivation for the melt inclusion study was to determine pre-eruptive water concentrations using Raman spectroscopy because of the importance of water in melt generation and crystallization (e.g. plagioclase stability). Because of the ease of hydrogen diffusion out of inclusions during heating runs, water concentrations were determined only on the unheated inclusions, but some diffusive water loss during magma ascent is still likely (Chen *et al.*, 2013). The water concentrations in all inclusions are low, ranging from 0·13 to 0·56 wt % H_2O (Table 8). For comparison, the host-rock sample RAN2 contains 0·89 wt % H_2O. The analyses of inclusion glasses by electron microprobe (Table 8) reveal that the unheated, glassy inclusions have lower Mg# (41–44) than the homogenized ones (63–64). Only the latter show reasonable agreement with the whole-rock composition (Mg# = 69), and are consistent with equilibrium Mg–Fe partitioning with the olivine (K_D = 0·28–0·30). We attribute the low Mg# and low K_D values of the unheated, glassy inclusions to the effects of olivine precipitation on the inclusion walls during cooling, which was at least partly remelted in the heating experiments. Reverse fractionation modeling (olivine addition) using the PETROLOG program (Danyushevksy *et al.*,

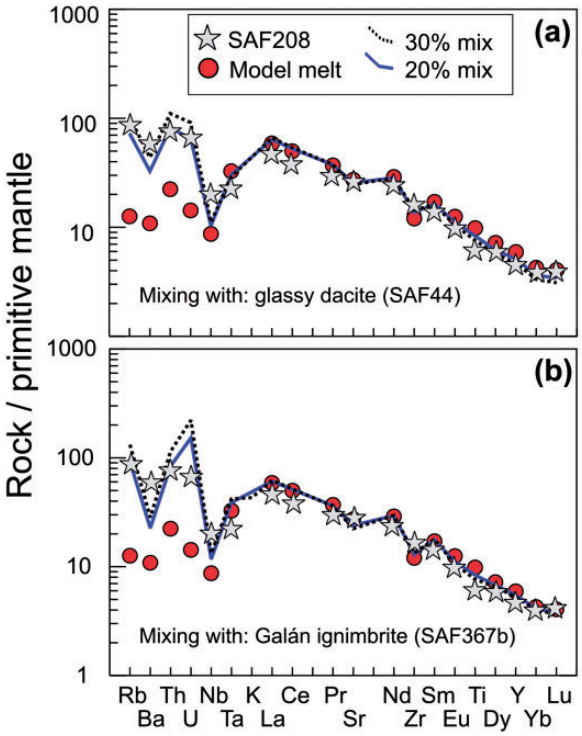

Fig. 13. Mixing models (dashed and continuous lines) to explain the mismatch between the calculated model melts from clinopyroxene trace elements (dots) and the bulk-rock (stars) for sample SAF208. (a) Mixing model for glassy dacite SAF44 shows a good fit for all elements with 20% assimilation); (b) mixing model for Galán rhyodacite SAF367b has too low Ba and too high U and Th to fit the data.

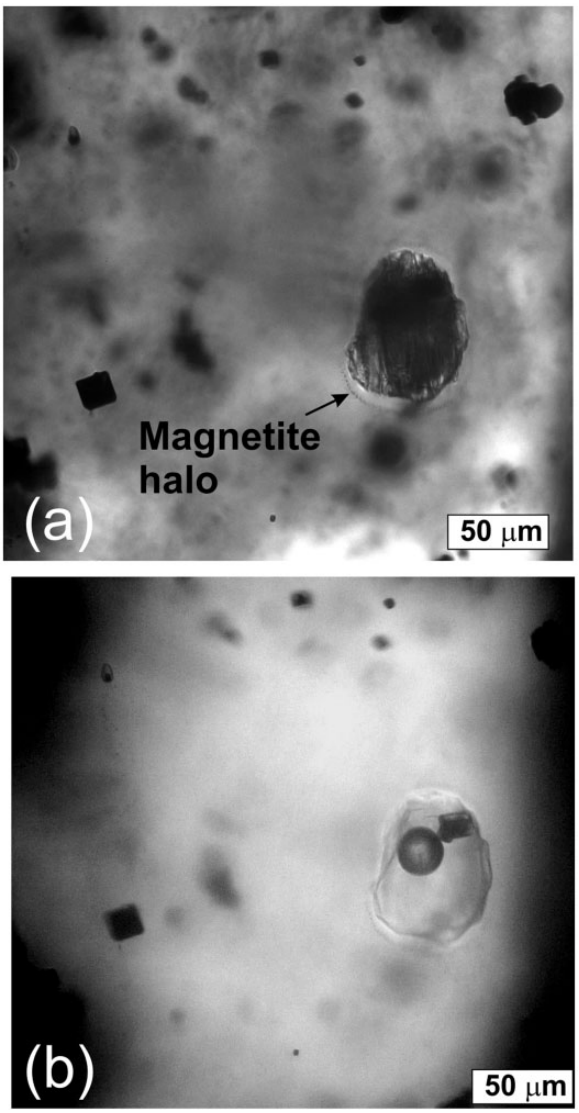

Fig. 14. Photomicrographs of a devitrified melt inclusion in olivine from sample RAN2, before (a) and after (b) reheating to 1250°C at 1 atm. The gas bubble visible in (b) failed to dissolve into the melt owing to the low pressure of the heating experiment. The spinel crystal in the reheated inclusion (b) was accidentally trapped and is not a daughter phase. The halo of opaque crystals (Fe-rich, presumed magnetite) around the lower end of the melt inclusion in (a) is attributed to water loss after trapping and oxidation of the olivine host.

2002) indicates that the glassy inclusions may have undergone 8–11 wt % olivine loss by post-trapping crystallization. The comparison of major element compositions in olivine-adjusted glassy inclusions and homogenized inclusions show good agreement (Table 8, Fig. 15), the remaining differences being slightly higher Al_2O_3 and CaO, and lower FeO and MgO in the adjusted glassy inclusions. These may be due to imperfect adjustment for post-trapping crystallization and re-equilibration, and the presence of clinopyroxene daughter crystals suggests that the adjustment by olivine addition alone is not completely appropriate for these melts.

The comparison of melt inclusion compositions with that of the host-rock RAN2 and other samples of the mafic suite shows several important differences (Fig. 15). The SiO_2 contents and Mg# are nearly the same in host-rock and melt inclusions, but the inclusions have lower MgO and FeO, and higher CaO and Al_2O_3 (Fig. 15). Contrary to expectation, the olivine-hosted melt inclusions in this sample are more evolved than the bulk-rock in terms of Mg and Fe, and furthermore, the inclusions do not lie on the variation trend defined by the mafic suite (dashed arrows, Fig 15). The normalized trace element patterns of the melt inclusions (Fig. 15d) show good agreement with the host-rock and other members of the mafic suite. It should be noted that the element concentrations in glassy inclusions are systematically higher than in the homogenized melt inclusions and in the bulk-rocks. This difference is likely to result from post-entrapment olivine crystallization on the inclusion walls, increasing the incompatible element concentrations in the remaining liquid. The difference in average trace element contents between reheated and glassy groups of inclusions is 11–25%, which is in reasonable agreement with the 11% estimate for

Table 8: Composition of glassy and reheated devitrified melt inclusions in RAN2 olivine

Grain:	T46	T45	T42	T43	T50	T51	T52	T56	T44	T54	T55
	heated	heated	glassy	glassy	glassy	glassy	glassy	glassy	glassy	glassy	glassy
n:	4	2	2	2	7	3	2	5	1	3	3
wt %											
SiO_2	50·5	53·0	53·0	51·7	52·2	51·6	51·7	53·7	51·2	50·5	52·0
TiO_2	1·40	1·27	1·59	1·61	1·64	1·78	1·72	1·45	1·77	1·76	1·73
Al_2O_3	18·90	17·9	20·7	21·3	21·3	21·6	21·3	21·4	21·5	21·3	21·3
FeO_{tot}	6·50	5·87	3·25	3·94	3·92	3·70	3·15	3·53	3·38	3·98	3·47
MnO	b.d.	b.d.	b.d.	b.d.	b.d.	b.d.	0·08	b.d.	b.d.	b.d.	b.d.
MgO	6·37	5·52	1·46	1·55	1·75	1·37	1·30	1·52	1·30	1·65	1·55
CaO	9·9	9·6	11·1	11·8	11·5	12·4	11·9	10·6	12·2	12·2	12·4
Na_2O	3·66	3·81	4·16	4·00	4·13	4·50	4·27	4·09	4·34	4·10	4·13
K_2O	1·73	1·77	2·09	1·94	2·05	2·09	2·10	2·05	2·00	1·99	2·03
P_2O_5	0·28	0·26	0·27	0·36	0·34	0·40	0·36	0·34	0·40	0·35	0·35
Total	98·3	99·1	97·6	98·3	98·8	99·4	97·9	98·7	98·1	97·9	98·9
Cl	0·16	0·15	0·16	0·18	0·18	0·19	0·16	0·16	0·20	0·19	0·18
H_2O	–	–	–	–	0·29	0·14	0·56	0·37	0·27	0·39	0·30
Mg#	64	63	44	41	44	43	42	44	41	42	44
Fe_2O_3*	0·72	0·65	0·36	0·44	0·44	0·36	0·35	0·39	0·38	0·44	0·39
FeO	5·85	5·28	2·93	3·54	3·52	2·91	2·84	3·18	3·04	3·58	3·12
Host olivine											
Fo (mol %)	87·4	85·8	87·6	86·7	88·6	88·0	86·9	86·0	88·1	87·8	88·0
wt % corrected for crystallization of host olivine†											
SiO_2	–	–	53·2	51·4	51·4	51·1	51·8	53·3	51·0	50·4	51·4
TiO_2	–	–	1·51	1·49	1·49	1·66	1·63	1·36	1·64	1·62	1·60
Al_2O_3	–	–	19·6	19·7	19·4	20·1	20·2	20·2	19·9	19·7	19·7
FeO	–	–	3·74	4·56	4·43	3·70	3·66	3·97	4·03	4·55	3·93
Fe_2O_3	–	–	0·70	0·84	0·83	0·73	0·70	0·71	0·78	0·87	0·76
MnO	–	–	–	–	–	–	0·08	–	–	–	–
MgO	–	–	4·69	5·30	6·03	4·70	4·30	4·38	5·18	5·70	5·09
CaO	–	–	10·5	10·9	10·5	11·5	11·3	9·97	11·3	11·3	11·4
Na_2O	–	–	3·94	3·70	3·76	4·18	4·04	3·85	4·01	3·78	3·83
K_2O	–	–	1·98	1·79	1·86	1·95	1·99	1·93	1·85	1·84	1·88
P_2O_5	–	–	0·26	0·33	0·31	0·37	0·34	0·32	0·37	0·32	0·32
Cl	–	–	0·15	0·16	0·16	0·18	0·15	0·15	0·18	0·17	0·16
H_2O	–	–	–	–	0·26	0·13	0·52	0·34	0·24	0·35	0·28
Mg#	–	–	66	64	68	66	64	63	66	66	66
Trace elements (ppm)											
Ba	408	367	599	456	–	–	–	–	–	–	–
Rb	29	25	37	31	–	–	–	–	–	–	–
Sr	676	681	817	800	–	–	–	–	–	–	–
Th	5·7	3·8	8·3	5·2	–	–	–	–	–	–	–
Nb	22	18	28	24	–	–	–	–	–	–	–
Zr	182	157	224	204	–	–	–	–	–	–	–
Y	23	23	28	27	–	–	–	–	–	–	–
La	32	25	41	36	–	–	–	–	–	–	–
Ce	67	56	85	75	–	–	–	–	–	–	–
Sm	5·9	5·0	7·3	6·3	–	–	–	–	–	–	–
Eu	1·5	1·3	2·0	1·7	–	–	–	–	–	–	–
Gd	6·6	6·2	7·8	7·0	–	–	–	–	–	–	–
Dy	4·5	4·2	5·7	4·9	–	–	–	–	–	–	–
Er	2·4	2·3	3·1	2·5	–	–	–	–	–	–	–
Yb	2·2	2·1	1·9	1·5	–	–	–	–	–	–	–

Major element analysis by electron microprobe, water by laser Raman spectroscopy, trace elements by SIMS. Computations used PETROLOG 2.1 (Danyushevsky *et al.*, 2002) for 0·8 GPa pressure. $Mg\# = 100\,Mg/(Mg + Fe^{2+})$ molar with Fe^{2+} estimated as above.
*Fe^{2+}/Fe^{3+} in the melt (1 atm) is calculated from spinel compositions in the host olivine following Maurel & Maurel (1982).
†Equilibrium olivine is added incrementally until a composition in equilibrium with the host crystal is reached.

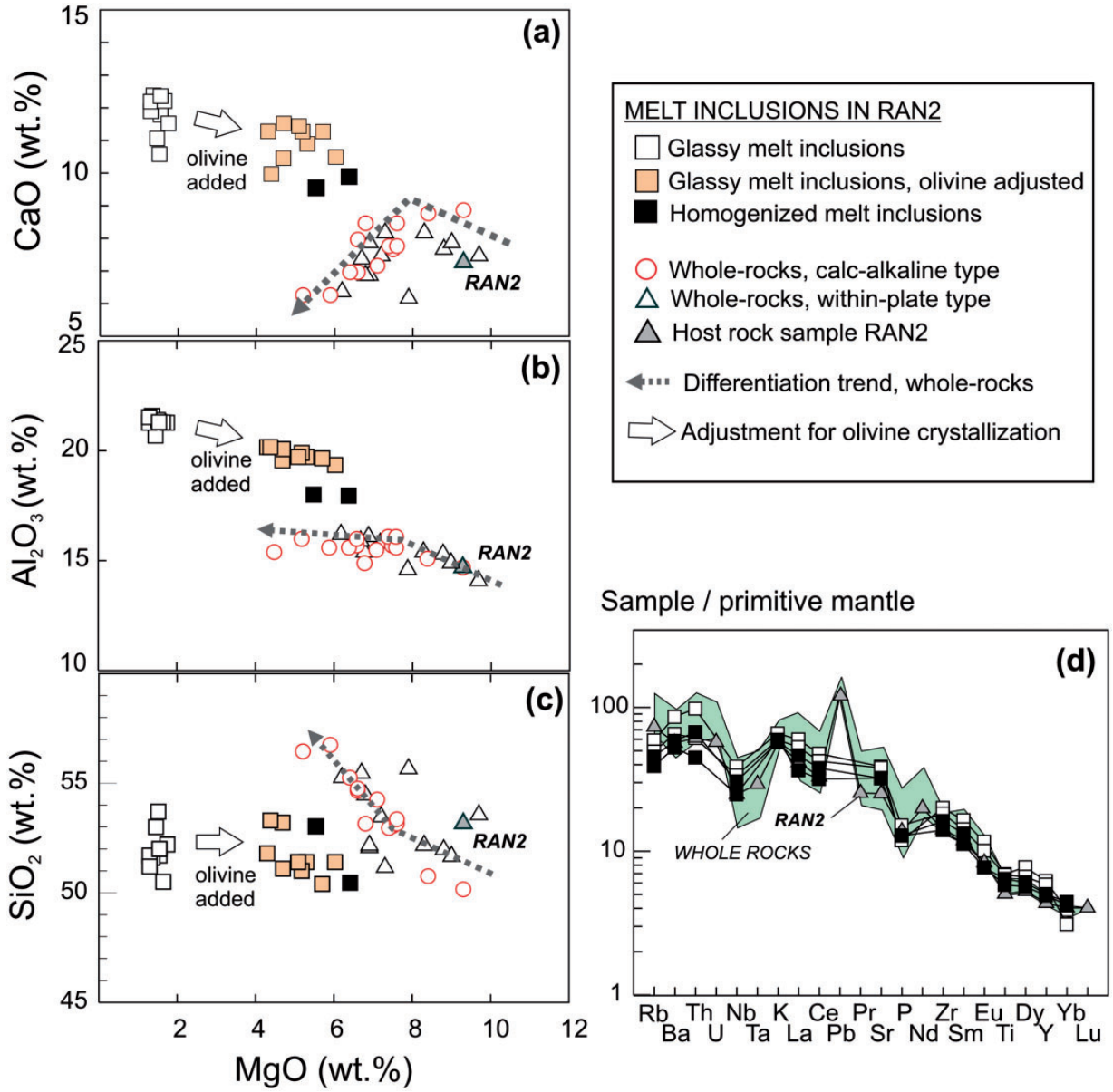

Fig. 15. (a–c) Variation of CaO, Al_2O_3 and SiO_2 in melt inclusions vs wt % MgO. The various symbols denote analyses of glassy (raw data and olivine-adjusted) and homogenized (reheated) inclusions. Comparison of bulk-rock data with qualitative differentiation trends (dashed lines, not modeled) shows that the melt inclusions are offset towards high Al and high Ca values (see text). (d) Primitive mantle normalized trace element compositions of melt inclusions, host-rock RAN2 and other members of the mafic suite (shaded field). Primitive mantle values from Sun & McDonough (1989).

olivine crystallization estimated by major-element modeling with PETROLOG. The REE analyses of melt inclusions indicate at first glance that the trapped melts have a negative Eu anomaly (Eu/Eu* = 0·70–0·80; compared with 0·87 for the host-rock). Unfortunately, there is a large uncertainty in the Eu analyses by SIMS (*c.* 40%), meaning that a value of 0·7 for Eu/Eu* cannot be distinguished with certainty from unity.

In many ways, the melt inclusion compositions resemble high-aluminum basalts (Al_2O_3 contents of 18–20 wt % at 5–6 wt % MgO and 51 wt % SiO_2). High-aluminum basalts are common in many volcanic arcs (e.g. Sisson & Grove, 1993; Kay & Kay, 1994) including the Southern Volcanic Zone of the Andes (e.g. Hickey *et al.*, 1986; Tormey *et al.*, 1991), but they have not been recognized in the Central Volcanic Zone. Given the small number of inclusions studied and the single sample hosting them, it is premature to discuss the origin and significance of these high-Al compositions in detail. Nevertheless, the observations and data from the melt inclusions in RAN2 are

valid, and they suggest that high-Al basalt is a minor component of the southern Puna magmatism, too small perhaps to erupt as lavas. Many studies of basaltic systems have shown that melt inclusions can reveal features of magma diversity not seen in the bulk-rocks (e.g. Yaxley *et al.*, 2004; Keiding *et al.*, 2011; Laubier *et al.*, 2012).

There is an interesting similarity between our findings in the Puna back-arc and observations of high-Al, high-Ca melt inclusions in olivine from mid-ocean ridge basalt (MORB; Laubier *et al.*, 2012), although in the latter case the high-Al melts are part of a wide range of inclusion compositions. Laubier *et al.* (2012) suggested that the melt inclusions in MORB olivines in their study represent small and discrete fractions of liquid from a complex melting column beneath the mid-ocean ridge. Different compositional groups of inclusions reflect different degrees of melting at different depths, variable melt–rock interactions and partial pooling (mixing). The high-Al basalt component in that case was attributed to assimilation of plagioclase-rich cumulus material, evidenced by positive Sr anomalies. The trace element patterns of melt inclusions in Puna sample RAN2 show a slight peak at Sr, and the inclusions are enriched in Sr relative to the host-rock (680 vs 530 ppm) so plagioclase assimilation might have played a role—possibly in the lower crust.

There are other models for high-Al basalts including high-pressure fractionation (e.g. Kay & Kay, 1994), which may be appropriate for the thick Andean crust. However, without many more melt inclusion observations from more samples, any interpretation is speculative. It is puzzling why only one of the 28 samples bearing olivine phenocrysts has melt inclusions and why all of the inclusions in RAN2 ($n = 34$) have high-Al characteristics that are completely lacking in the whole-rock suite. It appears that the melt trapped in RAN2 olivines represented a distinct liquid, more evolved and with a different history from the bulk magma. Being more evolved than the bulk magma, and possibly having assimilated plagioclase-rich material, the high-Al melt may be of lower temperature and its introduction to the RAN2 magma perhaps caused a hiatus in olivine crystallization or even partial resorption, which favored trapping of inclusions from the foreign melt. If such a process took place, it left no textural evidence in the host olivine grains.

DISCUSSION: TWO STAGES OF MAGMA EVOLUTION

Primary magmas and the nature of the mantle beneath the southern Puna

The major element composition of the primary magmas of the mafic suite can be derived from petrological modeling of the major element compositions as implemented in the PRIMELT2 program of Herzberg & Asimov (2008). The procedure searches for primary magma compositions consistent with observed rock compositions on the one hand, and with melts of peridotite mantle on the other. The method assumes that the observed basaltic compositions evolved from primary melts via olivine fractionation only. This severely restricts its application to the Puna mafic suite, as most samples have variations in both CaO and MgO suggesting clinopyroxene fractionation as well. One composition that meets all requirements for applying PRIMELT2 is basalt P07SUR1-01 from Drew *et al.* (2009). The PRIMELT2 solution using this composition as a starting point predicts a primary melt (pooled fractional melting at ~2 GPa) with 47·4 wt % SiO_2 and 14·6 wt % MgO, and the model further indicates that this melt could result from 13% partial melting of a lherzolite source. Lee *et al.* (2009) developed similar procedures for estimating the composition and melting conditions of primary magmas from the observed compositions of basalts. Their method yields essentially the same results of 47·5% SiO_2 and 13·3% MgO for the primary magma, and suggests further that the P–T conditions of last equilibration of the magma with its mantle source were at 1·92 GPa (compare 2 GPa for PRIMELT2) and 1364°C. The pressure corresponds to a depth near 60 km, which is in accord with Moho depths in this region (Wölbern *et al.*, 2009; Bianchi *et al.*, 2013). The mantle potential temperature calculated from these results is 1470°C, which is at the upper end of temperatures suggested for the MORB-source asthenosphere (Putirka *et al.*, 2007).

Crustal assimilation in the arc magmas of the Central Andes is widespread and is a major challenge in understanding the nature of the mantle source (depleted vs enriched; asthenospheric vs lithospheric). The radiogenic isotopic composition of Cretaceous extension-related basalts from NE of the study area indicates the presence of depleted mantle under this region before the Andean orogeny (Kay *et al.*, 1994, 1999; Lucassen *et al.*, 2002; Fig. 5). The composition of Oligocene to early Miocene basaltic rocks in Bolivia and Chile also suggests a depleted mantle (Chiar Khollu basalt, Bolivia: Davidson & de Silva, 1995; Máquinas and Segerstrom basalts, Chile: Kay *et al.*, 1991, 1999). However, the radiogenic isotopic signatures of the late Miocene–Pliocene southern Puna mafic suite are clearly enriched (εNd −0·8 to −6 and $^{87}Sr/^{86}Sr$ from 0·705 to 0·709; Fig. 5). This can be explained by derivation of primary magmas from an enriched mantle source, or by later assimilation of enriched material from the crust or lithosphere. The variation in Sr and Nd isotope compositions and their correlation with SiO_2 or other differentiation indices is evidence for assimilation during magma evolution. However, it is important to recognize that the most primitive lavas already have enriched Nd and Sr isotopic compositions, and, furthermore, the high Sr concentrations in the primitive lavas argue strongly against

crustal assimilation to explain the radiogenic $^{87}Sr/^{86}Sr$ (e.g. Francis *et al.*, 1989; Rogers & Hawkesworth, 1989; Kay *et al.*, 1994, 1999, 2011, 2013; Drew *et al.*, 2009). An example illustrating this from our samples is RAN9 with 50·2 wt % SiO_2, 9·3 wt % MgO and 996 ppm Sr, which has values of $^{87}Sr/^{86}Sr = 0{\cdot}70527$ and $\varepsilon Nd = -0{\cdot}3$. The geochemically most primitive lava from the southern Puna yet described is Pasto Ventura P07SUR01-1 (Drew *et al.*, 2009), which has 47·5 wt % SiO_2, 10·3 wt % MgO, 785 ppm Sr, $^{87}Sr/^{86}Sr = 0{\cdot}70553$ and $\varepsilon Nd = -0{\cdot}7$. This comes very close to an estimated primary magma composition of 48 wt % SiO_2, 780 ppm Sr and $^{87}Sr/^{86}Sr = 0{\cdot}7045$ derived by Kay *et al.* (1994) from mixing calculations based on Sr and SiO_2 concentrations, Eu anomalies and the Sr isotope ratios of southern Puna lavas, Cretaceous basalts and a crustal contaminant similar to the glassy dacite (SAF44) described above.

We conclude that there must be an enriched mantle source for the southern Puna back-arc suite, but there are conflicting views on what this implies in terms of a geodynamic interpretation. Rogers & Hawkesworth (1989) suggested that the enriched isotopic signatures of the Neogene mafic magmas are due to a long-lived subcontinental mantle lithosphere beneath the Central Andes, but this is inconsistent with the depleted isotopic signatures of the Cretaceous lavas (Kay *et al.*, 1994; Lucassen *et al.*, 2002). Drew *et al.* (2009) proposed that the enriched isotopic signature of the Puna mafic suite results from a remnant of subcontinental lithospheric mantle that produced isotopically enriched magmas in the Ordovician Famatinian arc. They suggested that this enriched lithospheric remnant was caught between depleted lithospheric mantle to the east, which had been there since at least the Cretaceous, and a second region of depleted mantle to the west, like that which gave rise to the Jurassic arc lavas erupted in the coastal Cordillera. We note that depleted mantle to the west of the Puna is inconsistent with isotopic data for post 8 Ma lavas within and to the west of the modern CVZ, which indicate an enriched mantle source (Kay *et al.*, 1999; Goss & Kay, 2009). The near-primitive Pliocene and younger (<2 Ma) magmas from the west of our study area, like the Incahuasi basalts (Kay *et al.*, 1999; Kay, 2006), have ~49% SiO_2, 750 ppm Sr and initial $^{87}Sr/^{86}Sr$ ratios near 0·7055 very much like the southern Puna rocks. Rather than invoking piecemeal preservation of pre-existing, lithosphere blocks to explain the enriched isotope signature of the southern Puna lavas, we prefer the alternative view that depleted mantle was once pervasive and it became re-enriched since the early Miocene by the addition of crustal material into the mantle wedge owing to the well-established processes of subduction erosion of the forearc (Stern, 1991; Kay *et al.*, 1999, 2005, 2011, 2013; Kay & Mpodozis, 2002; Kukowski & Oncken, 2006; Goss & Kay, 2009) and by delamination (Kay *et al.*, 1994, 1999; Schurr *et al.*, 2006; Bianchi *et al.*, 2013). The high potential temperatures indicated for primary magmas in the southern Puna (see above) favor melt generation in the asthenospheric mantle and not in the continental lithosphere.

First-stage assimilation in the lower to middle crust

It was argued above that the enriched Sr and Nd isotopic composition of the most primitive basaltic samples from the southern Puna mafic suite is a feature of their mantle source, whatever its ultimate cause. However, this is only the starting point and crustal assimilation played a major role in the further evolution of the magmas during their ascent and storage before erupting. Evidence for this is the wide range in Sr and Nd isotope compositions and positive correlation of isotopic composition with silica content (e.g. inset in Fig. 5) and the presence of negative Eu anomalies in rocks lacking plagioclase phenocrysts. These arguments have been made before, but new, and perhaps the most compelling evidence for crustal assimilation comes from the oxygen isotope composition of olivine. Kay *et al.* (2011) determined $\delta^{18}O$ values of olivine separates from three samples included in this study (SAF32, SAF24, SAF76). These yielded values of +6·3, +6·4 and +6·8‰, respectively, which correspond to a melt composition of +6·7–7·2‰ based on an olivine–melt fractionation factor of −0·4 from Bindemann (2008). Mid-ocean ridge basalts and most island arc basalts have a very narrow range of $\delta^{18}O$ value of $+5{\cdot}7 \pm 0{\cdot}2$‰, which can be taken as the mantle value. Clearly, the southern Puna O isotope compositions are well above this range, indicating assimilation of crust by melts during or before the stage of olivine crystallization. Given an estimate of the crustal O isotope ratio, one can readily calculate the proportion of crustal material required. Kay *et al.* (2011) proposed a crustal composition of $\delta^{18}O = +11$‰ in the southern Puna from their study of Cerro Galán ignimbrites. On that basis, the proportions of crust in the three mafic samples are 16, 18 and 26%, respectively.

The pressures and temperatures estimated from mineral–melt equilibria in these samples do not preserve evidence for a lower-crustal stage of crystallization and assimilation, but the trend of Sr and Nd isotopic variations (Fig. 5) requires a crustal assimilant with low $^{143}Nd/^{144}Nd$ and only moderate $^{87}Sr/^{86}Sr$, much lower than that of exposed Paleozoic granitoids and metamorphic rocks (e.g. 0·75–0·85 at 5 Ma). The crustal component must have a low time-integrated Rb/Sr ratio, and a likely candidate is the high-grade felsic lower crust, which is known from granulite xenoliths in Salta Rift volcanic rocks studied by Lucassen *et al.* (1999). The inferred lower-crustal stage of assimilation was probably where a negative Eu anomaly was acquired by the mafic magmas, as we observe that the Eu/Eu* ratio correlates with initial Sr and

Nd isotope ratios. This presence of negative Eu anomalies in clinopyroxene requires that the magmas acquired this feature before the onset of clinopyroxene crystallization, which probably took place at mid-crustal depths between about 20 and 40 km (0·7–1 GPa).

Crystallization and assimilation in the mid- and upper crust

Evidence for a second and shallower stage of crustal assimilation in the mafic magmas comes from the mismatch between trace element contents in clinopyroxenes and their host-rocks, and is supported by the anomalous $MgO–SiO_2$ relations and local presence of resorbed quartz xenocrysts in some samples (Fig. 3d). The melt compositions calculated from clinopyroxene trace element contents and mineral–melt *D* values match the host-rock composition for most elements reasonably well, including Eu and the other REE (Figs 11 and 12). However, for Rb, Ba, U, Th and to a lesser extent Nb, the host-rocks have up to 10 times higher concentrations than the model melts. This implies that after crystallization of clinopyroxene, and presumably at higher crustal levels, the magmas underwent further assimilation of crustal material before eruption.

There is a large uncertainty in this assessment for Rb and Ba owing to their very low abundances in clinopyroxene or uncertain *D* values, but the same trends are also observed for U and Th (Fig. 11). Given the abundance of silicic volcanic rocks in the southern Puna with the same age range as the mafic suite, and the greater energy efficiency of assimilating melts rather than granitic basement, we postulate that the second-stage assimilation took place by magma mixing. Using mixing calculations (Fig. 13) we showed that the mismatch of model melts and bulk-rocks can be explained by about 20% assimilation of a dacitic melt.

CONCLUSIONS

The main compositional features and geodynamic importance of the <7 Ma back-arc mafic lavas in the southern Puna Plateau of the central Andes have been established previously (Kay *et al.*, 1994, 1999; Drew *et al.*, 2009). This study provides new constraints on the conditions of generation of the parental magmas in the mantle and on the temperatures and depths at which the mafic magmas interacted with the crust during their ascent. From a combination of bulk-rock compositions and petrological models based on mineral–melt geothermobarometry, trace element data from clinopyroxene and analysis of olivine-hosted melt inclusions, we reach the following main conclusions.

(1) The primary basaltic magmas originated from an enriched mantle source, in agreement with the conclusions of previous rersearchers (e.g. Rogers & Hawkesworth, 1989; Kay *et al.*, 1994). Based on the compositions of near-primitive back-arc basalts, the minimum initial $^{87}Sr/^{86}Sr$ and maximum $^{143}Nd/^{144}Nd$ ratios for the mantle source are near 0·705 and 0·5126, respectively. We argue that this mantle source does not represent pre-Mesozoic subcontinental lithosphere as proposed by Drew *et al.* (2009). High mantle potential temperatures (1470°C) favor an asthenospheric source that has been geochemically enriched by introduction of crustal material from forearc subduction erosion and lithospheric delamination during the Andean orogeny (e.g. Kay *et al.*, 1994, 2011, 2013).

(2) The water contents in the Puna mafic suite, indicated by primary olivine-hosted melt inclusions (<0·5 wt %) and whole-rock analyses (<1 wt % H_2O), are low compared with arc values, and the lack of typical trace element signatures indicative of slab fluid-enhanced melting is consistent with the cause of melting in the back-arc being decompression of upwelling asthenospheric mantle. Plausible scenarios for mantle upwelling in this setting are delamination of the lower crust and lithospheric mantle in the aftermath of crustal thickening (Kay *et al.*, 1994; Sobolev & Babeyko, 2005; Schurr *et al.*, 2006) and slab steepening after subduction of an aseismic ridge under the region (Kay & Coira, 2009).

(3) Petrological models (Lee *et al.*, 2009; Herzberg & Asimov, 2008) suggest that the compositions of pooled, near-primitive melts for the Puna mafic suite magmas are mildly alkaline basalts with 47–48 wt % SiO_2 and 13–15 wt % MgO. The mantle-derived magmas segregated at temperatures near 1364°C and depths of 60 km, in agreement with the Moho depth in this region and with seismic evidence for a zone of magma stagnation and pooling near the crust–mantle boundary (e.g. Wölbern *et al.*, 2009; Bianchi *et al.*, 2013).

(4) Geothermobarometric calculations based on olivine–melt and clinopyroxene–melt equilibria (core compositions) indicate phenocryst crystallization temperatures of ~1320–1220°C for olivine and ~1230–1140°C for clinopyroxene. The inferred crystallization sequence of olivine followed by clinopyroxene is consistent with thermodynamic modeling at mid-crustal pressures of ~0·7–1 GPa. This agrees with clinopyroxene barometry and correspond to depths of 20–35 km. Oxygen fugacity calculations based on spinel–melt equilibrium indicate relatively reducing conditions as much as 2 log units below the QFM buffer. The temperature values are higher than typical for continental arc lavas and the oxygen fugacity estimates are lower. Both of these differences are consistent with a magma origin by upwelling of

asthenosphere rather than by dehydration-enhanced melting of the mantle wedge above a subducting slab.

(5) The compositions of both olivine and clinopyroxene phenocrysts indicate that the mantle-derived magmas were contaminated in the lower part of the thick crust by assimilation of silicic melts before these phenocrysts crystallized. Evidence for prior assimilation comes from (a) oxygen isotopic ratios of olivine phenocrysts (Kay *et al.*, 2011) indicating non-mantle values of magma $\delta^{18}O$ from +6·7 to +7·2‰ and (b) negative Eu anomalies in clinopyroxene from plagioclase-free host-rocks.

(6) Model melt compositions calculated from trace element distributions in clinopyroxene are lower than the host-rock compositions for the most incompatible elements U, Th, Nb and probably also Rb and Ba (data inconclusive). This suggests continued crustal assimilation after clinopyroxene crystallization. Geochemical models suggest assimilation of about 20 wt % silicic melt similar to the glassy dacites from the southern Puna described by Kay *et al.* (1994). The likely setting for this later assimilation is in a prominent zone of partial melting in the crust at *c.* 20 km depth consistent with seismic observations (Kay *et al.*, 2011).

(7) Olivine-hosted melt inclusions have compositions more evolved than the host-rock, resembling high-Al basalts. Erupted lavas of this composition are not known in the Central Volcanic Zone, but they commonly occur in the Andean Southern Volcanic Zone (e.g. Hickey *et al.*, 1986) and in other arcs. The melt-inclusion data suggest that high-Al, high-Ca melts were part of the spectrum of magmas generated in the southern Puna, but were perhaps not abundant enough to erupt as discrete magmas.

(8) Based on the bulk-rock Sr–Nd isotope and olivine O isotope composition, we estimate of the order of 15–25 wt % crustal assimilation in the petrogenesis of the erupted magmas, in agreement with previous work by Kay *et al.* (1994).

ACKNOWLEDGEMENTS

We thank Pablo Caffe (Jujuy) for his assistance and comradeship during field work. Thanks also go to Xiaohui Yuan and Ben Heit (Potsdam) for discussions on Puna geophysics, and Robert Kay (Cornell) for discussions on petrology. For their help with analytical work in Potsdam we are grateful to Sabine Tonn, Heike Rothe and Rudi Naumann (XRF and ICP-MS), Michael Wiedenbeck (SIMS), Dieter Rhede and Oona Appelt (microprobe), Ilya Veksler (melt inclusions) and Friedrich Lucassen (radiogenic isotopes). The laser ablation work at the University of Frankfurt was hosted by Professor Gerhard Brey and supervised by Dr Yann Lahaye. Thorough and constructive reviews by anonymous referees and editor Simon Turner greatly improved the presentation.

FUNDING

Financial support for this research comes from the Deutsche Forschungsgemeinschaft DFG in the SFB-267 program 'Deformation Processes in the Andes' and from US National Science Foundation EAR Grants (0126000 and 0538112).

SUPPLEMENTARY DATA

Supplementary data for this paper are available at *Journal of Petrology* online.

REFERENCES

Allmendinger, R. W. (1986). Tectonic development, southeastern border of the Puna Plateau, northwestern Argentine Andes. *Geological Society of America Bulletin* **97**, 1070–1082.

Allmendinger, R. W., Jordan, T. E., Kay, S. M. & Isacks, B. L. (1997). The evolution of the Altiplano–Puna Plateau of the central Andes. *Annual Review of Earth and Planetary Sciences* **25**, 139–174.

Alonso, R., Viramonte, J. & Gutiérrez, R. (1984). Puna Austral—Bases para el subprovincialismo geologico de la Puna Argentina. *Noveno Congreso Geologico Argentino Actas* 43–63.

Ariskin, A. A., Frenkel, M. Y. & Barmina, G. S. (1993). COMAGMAT: a Fortran program to model magma differentiation processes. *Computers and Geosciences* **19**, 1155–1170.

Beattie, P. (1993). Olivine–melt and orthopyroxene–melt equilibria. *Contributions to Mineralogy and Petrology* **115**, 103–111.

Bedard, J. H. (1994). A procedure for calculating the equilibrium distribution of trace elements among the minerals of cumulate rocks, and the concentration of trace elements in the coexisting liquids. *Chemical Geology* **118**, 143–153.

Bianchi, M., Heit, B., Jakovlev, A., Yuan, X., Kay, S. M., Sandvol, E., Alonso, R. N., Coira, B., Brown, L., Kind, R. & Compte, D. (2013). Teleseismic tomography of the southern Puna plateau in Argentina and adjacent regions. *Tectonophysics* **586**, 65–83.

Bindeman, I. (2008). Oxygen isotopes in mantle and crustal magmas as revealed by single crystal analysis. In: Putirka, K. D. & Tepley, F. J., III (eds) *Minerals, Inclusions and Volcanic Processes. Mineralogical Society of America and Geochemical Society, Reviews in Mineralogy and Geochemistry* **69**, 445–478.

Boudreau, A. E. (1999). PELE—A version of the MELTS software program for the PC platform. *Computers and Geosciences* **25**, 21–203.

Cahill, T. & Isacks, B. L. (1992). Seismicity and shape of the subducted Nazca plate. *Journal of Geophysical Research* **97**, 17503–17529.

Chen, Y., Provost, A., Schiano, P. & Cluzel, N. (2013). Magma ascent rate and initial water concentration inferred from diffusive water loss from olivine-hosted melt inclusions. *Contributions to Mineralogy and Petrology* **165**, 525–541.

Clyne, M. A. & Borg, L. E. (1997). Olivine and chromian spinel in primitive calc-alkaline and tholeiitic lavas from the southernmost Cascade Range, California: a reflection of relative fertility of the source. *Canadian Mineralogist* **35**, 453–472.

Coira, B. & Kay, S. M. (1993). Implications of Quaternary volcanism at Cerro Tuzgle for crustal and mantle evolution of the Puna

Plateau, Central Andes, Argentina. *Contributions to Mineralogy and Petrology* **113**, 40–58.

Coira, B. & Pezzutti, N. (1976). Vulcanismo cenozoico en el ámbito de La Puna catamarqueña (25°30'–25°50' Lat. S. y 68°–68°30' Long. O.). *Asociación Geológica Argentina Revista* **31**, 33–52.

Coira, B., Kay, S. M. & Viramonte, J. (1993). Upper Cenozoic magmatic evolution of the Argentine Puna—A model for changing subduction geometry. *International Geology Review* **35**, 677–720.

Danyushevsky, L. V., McNeill, A. W. & Sobolev, A. V. (2002). Experimental and petrological studies of melt inclusions in phenocrysts from mantle-derived magmas: an overview of techniques, advantages and complications. *Chemical Geology* **183**, 5–24.

Davidson, J. P. & de Silva, S. L. (1992). Volcanic rocks from the Bolivian Altiplano: Insights into crustal structure, contamination, and magma genesis in the central Andes. *Geology* **20**, 1127–1130.

Davidson, J. P. & de Silva, S. L. (1995). Late Cenozoic magmatism of the Bolivian Altiplano. *Contributions to Mineralogy and Petrology* **119**, 387–408.

Déruelle, B. (1991). Petrology of Quaternary shoshonitic lavas of northwestern Argentina. In: Harmon, R. S. & Rapela, W. (eds) *Andean Magmatism and its Tectonic Setting. Geological Society of America, Special Papers* **265**, 201–216.

Dorais, M. J. & Tubrett, M. (2008). Identification of a subduction zone component in the Higganum dike, Central Atlantic Magmatic Province: A LA-ICPMS study of clinopyroxene with implications for flood basalt petrogenesis. *Geochemistry, Geophysics, Geosystems* **9**, doi:10.1029/2008GC002079.

Drew, S. T., Ducea, M. N. & Schoenbohm, L. M. (2009). Mafic volcanism on the Puna plateau, NW Argentina: Implications for the lithospheric composition and evolution with an emphasis on lithospheric foundering. *Lithosphere* **1**, 305–318.

Droop, G. T. R. (1987). A general equation for estimating Fe^{3+} concentrations in ferromagnesian silicates and oxides from microprobe analyses, using stoichiometric criteria. *Mineralogical Magazine* **51**, 431–435.

Dulski, P. (2001). Reference materials for geochemical studies: New analytical data by ICP-MS and critical discussion of Reference Values. *Geostandards Newsletter* **25**, 87–125.

Folkes, C. B., Wright, H. M., Cas, R. A. F., deSilva, S. L., Lesti, C. & Viramonte, J. G. (2011). A re-appraisal of the stratigraphy and volcanology of the Cerro Galán volcanic system, NW Argentina. *Bulletin of Volcanology* **73**, 1427–1454.

Francis, P. W., Sparks, R. S. J., Hawkesworth, C. J., Thorpe, R. S., Pyle, D. M., Tait, S. R., Mantovani, M. S. & McDermott, F. (1989). Petrology and geochemistry of volcanic rocks of the Cerro Galán caldera, northwest Argentina. *Geological Magazine* **126**, 515–547.

Goss, A. R. & Kay, S. M. (2009). Extreme high field strength element (HFSE) depletion and near-chondritic Nb/Ta ratios in Central Andean adakite-like lavas (~27°S, ~68°W). *Earth and Planetary Science Letters* **270**, 97–109.

Herzberg, C. & Asimov, P. D. (2008). Petrology of some oceanic island basalts: PRIMELT2.XLS software for primary magma calculation. *Geochemistry, Geophysics, Geosystems* **9**, doi:10.1029/2008GC002057.

Herzberg, C. & O'Hara, M. J. (2002). Plume-associated ultramafic magmas of Phanerozoic age. *Journal of Petrology* **43**, 1857–1883.

Herzberg, C., Asimow, P. D., Arndt, N., Niu, Y., Lesher, C. M., Fitton, J. G., Cheadle, M. J. & Saunders, A. D. (2007). Temperatures in ambient mantle and plumes: Constraints from basalts, picrites, and komatiites. *Geochemistry, Geophysics, Geosystems* **8**, doi:10.1029/2006GC001390.

Hickey, R. L., Frey, F. A., Gerlach, D. C. & Lopez-Escobar, L. (1986). Multiple sources for basaltic rocks from the southern zone of the Andes (34°–41°S): Trace element and isotopic evidence for contributions from subducted oceanic crust, mantle, and continental crust. *Journal of Geophysical Research* **91**, 5963–5983.

Hoke, L. & Lamb, S. (2007). Cenozoic behind-arc volcanism in the Bolivian Andes, South America: implications for mantle melt generation and lithospheric structure. *Journal of the Geological Society, London* **164**, 795–814.

Holloway, J. R. & Blank, J. G. (1994). Application of experimental results to C–O–H species in natural melts. In: Carroll, M. R. & Holloway, J. R. (eds) *Volatiles in Magmas. Mineralogical Society of America, Reviews in Mineralogy* **30**, 187–230.

Isacks, B. L. (1988). Uplift of the central Andean plateau and bending of the Bolivian orocline. *Journal of Geophysical Research* **93**, 3211–2231.

Jochum, K. P., Dingwell, D. B. *et al.* (2000). The preparation and preliminary characterization of eight geological MPI-DING reference glasses for *in-situ* microanalyses. *Geostandards Newsletter* **24**, 87–133.

Kay, R. W. & Kay, S. M. (1993). Delamination and delamination magmatism. *Tectonophysics* **219**, 177–189.

Kay, S. M. (2006). Chemical and isotopic evidence for modification of the Central Andean arc mantle by crust removed by forearc subduction erosion. *Geochimica et Cosmochimica Acta* **170**, A385.

Kay, S. M. & Abruzzi, J. (1996). Magmatic evidence for Neogene lithospheric evolution of the central Andean 'flat-slab' between 30°S and 32°S. *Tectonophysics* **259**, 15–28.

Kay, S. M. & Coira, B. (2009). Shallowing and steepening subduction zones, continental lithospheric loss, magmatism and crustal flow under the central Andean Altiplano–Puna plateau. In: Kay, S. M., Ramos, V. A. & Dickinson, W. R. (eds) *Backbone of the Americas. Shallow Subduction, Plateau Uplift and Ridge and Terrane Collision. Geological Society of America, Memoirs* **204**, 229–260.

Kay, S. M. & Kay, R. W. (1994). Aleutian magmatism in space and time. In: Plafker, G. & Jones, D. L. (eds) *The Geology of Alaska. Geological Society of America, Decade of North American Geology* **G-1**, 687–722.

Kay, S. M. & Mpodozis, C. (2002). Magmatism as a probe to the Neogene shallowing of the Nazca plate beneath the modern Chilean flat-slabs. *Journal of South American Earth Sciences* **15**, 39–57.

Kay, S. M., Mpodozis, C., Ramos, V. A. & Munizaga, F. (1991). Magma source variations for mid–late Tertiary magmatic rocks associated with a shallowing subduction zone and a thickening crust in the central Andes (28 to 33°S). In: Harmon, R. S. & Rapela, C. W. (eds) *Andean Magmatism and its Tectonic Setting. Geological Society of America, Special Papers* **265**, 113–137.

Kay, S. M., Coira, B. & Viramonte, J. (1994). Young mafic back arc volcanic rocks as indicator of continental lithospheric delamination beneath the Argentine Puna plateau, central Andes. *Journal of Geophysical Research* **99**, 24323–24339.

Kay, S. M., Mpodozis, C. & Coira, B. (1999). Neogene magmatism, tectonism, and mineral deposits of the Central Andes (22° to 33° latitude). In: Skinner, B. J. (ed.) *Geology and Ore Deposits of the Central Andes. Society of Economic Geology, Special Publication* **7**, 27–59.

Kay, S. M., Godoy, E. & Kurtz, A. (2005). Episodic arc migration, crustal thickening, subduction erosion, and magmatism in the south–central Andes. *Geological Society of America Bulletin* **117**, 67–88.

Kay, S. M., Coira, B. L., Caffe, P. J. & Chen, C.-H. (2010). Geochemical diversity, crustal and mantle sources and evolution of the Neogene Puna plateau ignimbrites of the Central Andes. *Journal of Volcanology and Geothermal Research* **198**, 81–111.

Kay, S. M., Coira, B., Woerner, G., Kay, R. W. & Singer, B. S. (2011). Geochemical, isotopic and single crystal $^{40}Ar/^{39}Ar$ age constraints on the evolution of the Cerro Galán ignimbrites. *Bulletin of Volcanology* **73**, 1487–1511.

Kay, S. M., Mpodozis, C. & Gardeweg, M. (2013). Magma sources and tectonic setting of Central Andean andesites (25·5–28°S) related to crustal thickening, forearc subduction erosion and delamination. In: Gomez-Tuena, A., Straub, S. M. & Zellmer, G. F. (eds) *Orogenic Andesites and Crustal Growth. Geological Society, London, Special Publications* (in press).

Keiding, J. K., Trumbull, R. B., Veksler, I. V. & Jerram, D. A. (2011). On the significance of ultra-magnesian olivines in basaltic rocks. *Geology* **39**, 1095–1098.

Kent, A. J. R., Baker, J. A. & Wiedenbeck, M. (2002). Contamination and melt aggregation processes in continental flood basalts: Constraints from melt inclusions in Oligocene basalts from Yemen. *Earth and Planetary Science Letters* **202**, 577–594.

Kilian, R. & Behrmann, J. H. (2003). Geochemical constraints on the sources of Southern Chile Trench sediments and their recycling in arc magmas of the Southern Andes. *Journal of the Geological Society, London* **160**, 57–70.

Knox, W. J., Kay, S. M. & Coira, B. (1989). Geochemical evidence on the origin of Quaternary basaltic andesites of the Puna, northwestern Argentina. *Asociacion Geológica Argentina, Revistas* **XLIV**, 194–206.

Kraemer, B., Adelmann, D., Alten, M., Schnurr, W., Erpenstein, K., Kiefer, E., van den Bogaard, P. & Görler, K. (1999). Incorporation of the Paleogene foreland into the Neogene Puna plateau: The Salar de Antofalla area, NW Argentina. *Journal of South American Earth Sciences* **12**, 157–182.

Kukowski, N. & Oncken, O. (2006). Subduction erosion—the 'normal' mode of fore-arc material transfer along the Chilean margin? In: Oncken, O., Chong, G., Franz, G., Giese, P., Götze, H.-J., Ramos, V. A., Strecker, M. R. & Wigger, P. (eds) *The Andes, Active Subduction Orogeny*. Springer, pp. 217–236.

Lahaye, Y., Lambert, D. & Walters, S. (1997). Ultraviolet laser sampling and high resolution inductively coupled plasma mass spectrometry of NIST and BCR-2G glass reference materials. *Geostandards Newsletter* **21**, 205–214.

Laubier, M., Gale, A. & Langmuir, C. H. (2012). Melting and crustal processes at the FAMOUS segment (Mid-Atlantic Ridge): new insights from olivine-hosted melt inclusions from multiple samples. *Journal of Petrology* **53**, 665–698.

LeBas, M. J., LeMaitre, R. W., Streckeisen, A. & Zanetti, B. (1986). A chemical classification of volcanic rocks based on the total alkali–silica diagram. *Journal of Petrology* **27**, 745–750.

Lee, C.-T. A., Luffi, P., Plank, T., Dalton, H. & Leeman, W. P. (2009). Constraints on the depths and temperatures of basaltic magma generation on Earth and other terrestrial planets using new thermobarometers for mafic magmas. *Earth and Planetary Science Letters* **279**, 20–33.

Lehnert, K., Su, Y., Langmuir, C., Sarbas, B. & Nohl, U. (2000). A global geochemical database structure for rocks. *Geochemistry, Geophysics, Geosystems* **1**, doi:10.1029/1999GC000026.

Liang, X., Sandvol, E. A., Brown, L. D., Heit, B., Yuan, X., Mulcahy, P. & Kay, S. M. (2011). The Q images of southern Puna plateau from body wave attenuation tomography. *American Geophysical Union Fall Meeting, San Francisco, 5–9 December 2013*, Abstract S51C-2226.

Lucassen, F., Lewerenz, S., Franz, G., Viramonte, J. & Metzger, K. (1999). Metamorphism, isotopic ages and composition of lower crustal granulite xenoliths from the Cretaceous Salta Rift, Argentina. *Contributions to Mineralogy and Petrology* **134**, 325–341.

Lucassen, F., Becchio, R., Harmon, R., Kasemann, S., Franz, G., Trumbull, R., Wilke, H.-G., Romer, R. L. & Dulski, P. (2001). Composition and density model of the continental crust at an active continental margin—the central Andes between 21° and 27°S. *Tectonophysics* **341**, 195–223.

Lucassen, F., Escayola, M., Romer, R. L., Viramonte, J., Koch, K. & Franz, G. (2002). Isotopic composition of the late Mesozoic basic and ultrabasic rocks from the Andes (23–32°S)—implications for the Andean mantle. *Contributions to Mineralogy and Petrology* **143**, 336–349.

Mamani, M., Tassara, A. & Wörner, G. (2008). Composition and structural control of crustal domains in the central Andes. *Geochemistry, Geophysics, Geosystems* **9**, doi:10.1029/2007GC001925.

Marrett, R. A., Allmendinger, R. W., Alonso, R. N. & Drake, R. E. (1994). Late Cenozoic tectonic evolution of the Puna plateau and adjacent foreland, northwestern Argentine Andes. *Journal of South American Earth Sciences* **7**, 179–207.

Maurel, C. & Maurel, P. (1982). Etude experimentale de Lèquilibre Fe^{2+}-Fe^{3+} dans les spinelles chromiferes et les liquies silicates basiques coexistants. *Comptes-Rendus des Seances de l'Academie des Sciences, Serie 2: Mecanique-Physique, Chimie, Sciences de l' Univers, Science de la Terre*, pp. 209–212.

McGlashan, N., Brown, L. D. & Kay, S. M. (2008). Crustal thicknesses in the Central Andes from teleseismically recorded depth phase precursors. *Geophysics Journal International* **175**, 1013–1022.

Moscoso, R., Maksaev, V., Cuitiñno, L., Díaz, F., Koeppen, R., Tosdal, R., Cunningham, C., McKee, E. & Rytuba, J. (1993). El complejo volcánico Cerro Bravos, región de Maricunga, Chile: geología, alteración hidrotermal y mineralización. In: *Investigaciones de Metales Preciosos en el complejo volcánico neógeno–cuaternario de los Andes Centrales*, Servicio Geológico de Bolivia, La Paz, 131–165.

Nalpas, T., Dabard, M.-P., Ruffet, G., Vernon, A., Mpodozis, C., Loi, A. & Hérail, G. (2008). Sedimentation and preservation of the Miocene Atacama gravels in the Pedernales–Chañaral Area, Northern Chile: Climatic or tectonic control? *Tectonophysics* **459**, 161–173.

Niu, Y., Wilson, M., Humphreys, E. R. & O'Hara, M. J. (2011). The origin of intra-plate ocean island basalts (OIB): the lid effect and its geodynamic implications. *Journal of Petrology* **52**, 1443–1468.

Pearce, N. J. G., Perkins, W. T., Westgate, J. A., Gorton, M. P., Jackson, S. E., Neal, C. R. & Chenery, S. P. (1997). A compilation of new and published major and trace element data for NIST SRM 610 and NIST SRM 612 glass reference materials. *Geostandards Newsletter* **21**, 115–144.

Poustovetov, A. A. (2000). Numerical modeling of chemical equilibria between chromian spinel, olivine, and basaltic melt, with petrologic applications, PhD thesis, Queen's University, Kingston, ON, Canada.

Poustovetov, A. A. & Roeder, P. L. (2000). The distribution of Cr between basaltic melt and chromian spinel as an oxygen geobarometer. *Canadian Mineralogist* **39**, 309–317.

Putirka, K. (2008). Thermometers and barometers for volcanic systems. In: Putirka, K. D. & Tepley, F. J., III (eds) *Minerals, Inclusions and Volcanic Processes. Mineralogical Society of America and Geochemical Society, Reviews in Mineralogy and Geochemistry* **69**, 61–120.

Putirka, K., Mikaelian, H., Ryerson, F. & Shaw, H. (2003). New clinopyroxene–liquid thermobarometers for mafic, evolved, and volatile-bearing lava compositions, with application to lavas from Tibet and the Snake River Plain, Idaho. *American Mineralogist* **88**, 1542–1554.

Putirka, K. D., Perfit, M., Ryerson, F. J. & Jackson, M. G. (2007). Ambient and excess mantle temperatures, olivine thermometry, and active vs. passive upwelling. *Chemical Geology* **241**, 177–206.

Putirka, K., Ryerson, F. J., Perfit, M. & Ridley, W. I. (2011). Mineralogy and composition of the oceanic mantle. *Journal of Petrology* **52**, 279–313.

Richards, J. P. & Villeneuve, M. (2002). Characteristics of the late Cenozoic volcanism along the Archibarca lineament from Cerro Llullaillaco to Corrida de Cori, northwest Argentina. *Journal of Volcanology and Geothermal Research* **116**, 161–200.

Richards, J. P., Ullrich, T. & Kerrich, R. (2006). The late Miocene–Quaternary Antofalla volcanic complex, southern Puna, NW Argentina: Protracted history, diverse petrology, and economic potential. *Journal of Volcanology and Geothermal Research* **152**, 197–239.

Risse, A., Trumbull, R. B., Coira, B., Kay, S. M. & van den Bogaard, P. (2008). $^{40}Ar/^{39}Ar$ geochronology of basaltic volcanism in the back-arc region of the southern Puna plateau, Argentina. *Journal of South American Earth Science* **26**, 1–15.

Rogers, G. & Hawkesworth, C. (1989). A geochemical traverse across the north Chilean Andes: Evidence for crust generation from the mantle wedge. *Earth and Planetary Science Letters* **91**, 271–285.

Romer, R. L., Heinrich, W., Schröder-Smeibidl, B., Meixner, A., Fischer, C. O. & Schulz, C. (2005). Elemental dispersion and stable isotope fractionation during reactive fluid-flow and fluid immiscibility in the Bufa del Diente aureole, NE Mexico: Evidence from radiographies and Li, B, Sr, Nd, and Pb isotope systematics. *Contributions to Mineralogy and Petrology* **149**, 400–429.

Schoenbohm, L. M. & Strecker, M. R. (2009). Normal faulting along the southern margin of the Puna Plateau, northwest Argentina. *Tectonics* **28**, doi:10.1029/2008TC002341.

Schnurr, W. B. W., Risse, A., Trumbull, R. B. & Munier, K. (2006). Digital Geological Map of the Southern and Central Puna Plateau, NW Argentina. In: Oncken, O., Chong, G., Franz, G., Giese, P., Götze, H.-J., Ramos, V. A., Strecker, M. R. & Wigger, P. (eds) *The Andes, Active Subduction Orogeny*. Springer (data DVD).

Schnurr, W. B. W., Trumbull, R. B., Clavero, J., Hahne, K., Siebel, W. & Gardeweg, M. (2007). Twenty-five million years of felsic magmatism in the southern Central Volcanic Zone of the Andes: geochemistry and magma genesis of ignimbrites from 25–27°S, 67–72°W. *Journal of Volcanology and Geothermal Research* **166**, 17–46.

Schurr, B., Asch, G., Rietbrock, A. & Oncken, O. (2006). Evidence for lithospheric detachment in the central Andes from local earthquake tomography. *Tectonics* **415**, 203–223.

Siebel, W., Schnurr, W. B. W., Hahne, K., Kraemer, B., Trumbull, R. B., van den Bogaard, P. & Emmermann, R. (2001). Geochemistry and isotope systematics of small- to medium-volume Neogene–Quaternary ignimbrites in the southern central Andes: evidence for derivation from andesitic magma sources. *Chemical Geology* **171**, 213–237.

Sisson, T. W. & Grove, T. L. (1993). Temperatures and H_2O contents of low-MgO high-alumina basalts. *Contributions to Mineralogy and Petrology* **113**, 167–184.

Sobolev, S. V. & Babeyko, A. Y. (2005). What drives orogeny in the Andes? *Geology* **33**, 617–620.

Sobolev, A. V., Hofmann, A. W., Kuzmin, D. V., Yaxley, G. M., Arndt, N. T., Chung, S.-L., Danyushevsky, L. V., Elliot, T., Frey, F. A., Garcia, M. O., Gurenko, A. A., Kamenetsky, V. S., Kerr, A. C., Krivolutskay, N. A., Matvientkov, V. V., Nikogosian, I. K., Rocholl, A., Sigurdsson, I. A., Sushchevskaya, N. M. & Teklay, M. (2007). The amount of recycled crust in sources of mantle-derived melts. *Science* **316**, 412–417.

Sparks, R. S. J., Francis, P. W., Hamer, R. D., Pankhurst, R. J., O'Callaghan, L. O., Thorpe, R. S. & Page, R. (1985). Ignimbrites of the Cerro Galán Caldera, NW Argentina. *Journal of Volcanology and Geothermal Research* **24**, 205–248.

Stern, C. (1991). Role of subduction erosion in the generation of Andean magmas. *Geology* **19**, 78–81.

Straub, S. M., LaGatta, A. B., Martin-Del Pozzo, A. L. & Langmuir, C. H. (2008). Evidence from high-Ni olivines for a hybridized peridotite/pyroxenite source for orogenic andesites from the central Mexican Volcanic Belt. *Geochemistry, Geophysics, Geosystems* **9**, doi:10.1029/2007GC001583.

Sun, S. S. & McDonough, W. F. (1989). Chemical and isotopic systematics of oceanic basalts: implications for mantle composition and processes. In: Saunders, A. D. & Norry, M. J. (eds) *Magmatism in the Ocean Basins. Geological Society, London, Special Publications* **42**, 313–345.

Tait, S. (1992). Selective preservation of melt inclusion in igneous phenocrysts. *American Mineralogist* **77**, 146–155.

Thomas, R. (2000). Determination of water contents of granite melt inclusions by confocal laser Raman microprobe spectroscopy. *American Mineralogist* **85**, 868–872.

Thomas, R. & Davidson, P. (2007). Progress in the determination of water in glasses and melt inclusions with Raman spectroscopy: A short review. *Acta Petrologica Sinica* **23**, 15–20.

Thomas, R., Kamentsky, V. S. & Davidson, P. (2006). Laser Raman spectroscopic measurements of water in unexposed glass inclusions. *American Mineralogist* **91**, 467–470.

Tormey, D. R., Hickey-Vargas, R., Frey, F. A. & López-Escobar, L. (1991). Recent lavas from the Andean volcanic front (33 to 42°S); interpretations of along-arc compositional variations. In: Harmon, R. S. & Rapela, C. W. (eds) *Andean Magmatism and its Tectonic Setting. Geological Society of America, Special Papers* **265**, 57–78.

White, W. M. (2009). Geochemistry, an online textbook. Chapter 7, Trace elements. http://www.geo.cornell.edu/geology/classes/Chapters/Chapter07.pdf.

Whitman, D., Isacks, B. L., Chatelain, J.-L., Chiu, J.-M. & Perez, A. (1992). Attenuation of high-frequency seismic waves beneath the central Andean plateau. *Journal of Geophysical Research* **97**, 19929–19947.

Whitman, D., Isacks, B. L. & Mahlburg Kay, S. (1996). Lithospheric structure and along-strike segmentation of the central Andean plateau: Seismic Q, magmatism, flexure, topography and tectonics. *Tectonophysics* **259**, 29–40.

Wilson, A. D. (1955). A new method for the determination of ferrous iron in rocks and minerals. *Bulletin of the Geological Survey of Great Britain* **9**, 56–58.

Woerner, G., Moorbath, S. & Harmon, R. S. (1992). Andean Cenozoic volcanic centers reflect basement isotopic domains. *Geology* **20**, 1103–1106.

Wölbern, I., Heit, B., Yuan, X., Asch, G., Kind, R., Viramonte, J., Tawackoli, S. & Wilke, H. (2009). Receiver function images from the Moho and the slab beneath the Altiplano and Puna plateaus in the Central Andes. *Geophysical Journal International* **177**, 296–308.

Yaxley, G. M., Kamenetsky, V. S., Kamenetsky, M., Norman, M. D. & Francis, D. (2004). Origins of compositional heterogeneity in olivine-hosted melt inclusions from the Baffin Island picrites. *Contributions to Mineralogy and Petrology* **148**, 426–442.

Yuan, X., Sobolev, S. V. & Kind, R. (2002). Moho topography in the central Andes and its geodynamic implications. *Earth and Planetary Science Letters* **199**, 389–402.

Zinner, E. & Crozaz, G. (1986). A method for the quantitative measurement of rare-earth elements in the ion microprobe. *International Journal of Mass Spectrometry* **69**, 17–38.